International Journal of Heat and Mass Transfer 220 (2024) 124882

Contents lists available at ScienceDirect

International Journal of Heat and Mass Transfer

journal homepage: www.elsevier.com/locate/ijhmt

# Heat transfer and pressure drops during high heat flux flow boiling of low-GWP refrigerants in 200 μm-wide multi-microchannels

Gennaro Criscuolo [a,*], Luigi Pietro Maria Colombo [b], Baris Burak Kanbur [a,*], Wiebke Brix Markussen [a], Martin Ryhl Kærn [a]

[a] Department of Mechanical Engineering, Technical University of Denmark, 2800 Kongens Lyngby, Denmark
[b] Department of Energy, Politecnico di Milano, 20156 Milano, Italy

ARTICLE INFO

*Keywords:*
High heat flux
Low GWP
Pressure drops
Flow boiling
Microchannel
Thermal management
R1234yf
R1234ze(E)

ABSTRACT

Thermal management of electronics is continuously challenged by increasing heat fluxes to be dissipated at minimum power consumption. This study investigated the pressure drops and the heat transfer coefficient of two low-GWP refrigerants, R1234yf and R1234ze(E), during flow boiling at high heat fluxes. The test geometry comprised 25 parallel microchannels, 200 μm wide, 1200 μm deep and 1 cm long, nominally. Inlet orifices were used to stabilize the flow. A parametric analysis involving the mass flux and heat flux was conducted for nominal saturation temperatures of 30.5°C and 40.5°C, resulting in a maximum confinement number $N_{Conf}$ of 2.16 for R1234yf and 2.52 for R1234ze(E). As the applied heat flux was increased from low to near-critical values, the two-phase heat transfer transitioned from a heat-flux-dominated mode to a convection-dominated one. The flow finally approached dryout, which led to the critical heat flux upon further heating. The experimental results were analysed through a regression with relevant non-dimensional groups, in particular the confinement number, $N_{Conf}$, the equivalent wall Biot number, $Bi$, the boiling number, $Bo$, the convection number, $Co$, and the Weber number, $We$. It was shown that $Bo$ and $Bi$ had a major influence in the heat-flux-dominated region, while $Co$ and $N_{Conf}$ determined the performance in the convective region, mainly due to the establishment of an intermittent annular flow. The total channel pressure drops were evaluated through the experimental measurement of the pressure drops in the inlet-outlet manifold, and the orifices. Due to the short channel length and the high heat fluxes, the pressure drops were dominated by the momentum change contribution, which accounted for at least 60% of the total pressure drops in the lowest case. The flow-wise heat transfer coefficients and the channel pressure drops were compared with the predictions of existing correlations, showing generally a fair agreement.

## 1. Introduction

The continuous improvement in packaging capabilities by the manufacturers of electronic devices represents a great challenge for thermal management systems, which need to dissipate higher heat fluxes at a minimum carbon footprint. Due to the rising level of heat dissipation, flow boiling in small-scale heat sinks has been envisioned as one of the most promising solutions to accommodate high heat fluxes in electronics. In fact, by relying on the relatively large heat of vaporization, two-phase pumped loops offer high heat transfer coefficients, compact design and low operating mass flow rates [1]. Low mass flow rates can minimize pressure drop, reduce the pumping power and therefore can pave the way to energy efficiency and low carbon footprint for thermal management systems.

The great potential offered by thermal management with two-phase cooling loops has promoted many investigations aimed at comprehending the heat transfer mechanisms and the pressure drops behavior of boiling fluids in small-scale channels, often also referred to as microchannels. However, as reported in the literature [2], thermal-fluid phenomena during boiling in microchannels are complex and have not been understood completely yet. While in conventional channels a clear demarcation has been observed between the flow phenomena associated to a nucleation-dominated behavior and a convection-dominated one, the same has not been found for microchannels. In fact, high heat fluxes and confinement of the vapor phase can lead to flow phenomena that are not accounted for in the classic flow boiling methods [3,4]. These phenomena were identified as being the presence of elongated bubbles [5], strong flow instabilities due to vapor confinement [6] and

* Corresponding authors.
*E-mail address:* babukan@dtu.dk (B.B. Kanbur).

https://doi.org/10.1016/j.ijheatmasstransfer.2023.124882
Received 1 July 2023; Received in revised form 5 October 2023; Accepted 25 October 2023
Available online 16 November 2023

**Nomenclature**

*Abbreviations*

| | |
|---|---|
| CHF | Critical Heat Flux |
| CMOS | Complementary Metal-Oxide Semiconductor |
| CNC | Computer Numerical Control |
| GWP | Global Warming Potential |
| HFO | Hydro-Fluoro-Olefins |
| MAPE | Mean Absolute Percentage Error |
| MPE | Mean Percentage Error |
| PEEK | PolyEtherEtherKetone |
| PID | Process and Instruments Diagram |
| RMSE | Root Mean Squared Error |
| RTD | Resistance Thermal Detector |
| SD | Standard deviation |

*Greek letters*

| | |
|---|---|
| $\Delta$ | Variation |
| $\epsilon$ | Void fraction calculated with the homogeneous mixture model |
| $\eta$ | Fin efficiency parameter |
| $\psi$ | Two-phase heat transfer enhancement factor |
| $\rho$ | Density |
| $\sigma$ | Surface tension or standard deviation |

*Latin letters*

| | |
|---|---|
| $\dot{m}$ | Refrigerant mass flow rate |
| $\widetilde{z}$ | Flow-wise coordinate, discrete |
| $Bi$ | Wall Biot number, $hH_{\mathrm{ch}}^2/(w_{\mathrm{wall}}k_{\mathrm{Cu}})$ |
| $Bo$ | Boiling number, $q/(\Delta i_{\mathrm{fg}}G)$ |
| $Co$ | Convection number, $(1/x-1)^{0.8}(\rho_v/\rho_l)^{0.5}$ |
| $d$ | Thickness of the conduction layer |
| $D_h$ | Channel diameter |
| $f$ | Pressure drop factor |
| $G$ | Channel mass flux |
| $g$ | Gravitational acceleration |
| $H$ | Height |
| $h$ | Heat transfer coefficient |
| $i$ | Enthalpy |
| $k$ | Thermal conductivity |
| $L$ | Length |
| $m$ | Fin parameter |
| $N$ | Number of channels |
| $N_{\mathrm{Conf}}$ | Confinement number, $[\sigma/g(\rho_L-\rho_V)]^{0.5}/D_h$ |
| $Nu$ | Nusselt number |
| $p$ | Pressure |
| $q$ | Heat flux |
| $Re$ | Reynolds number |
| $T$ | Temperature |
| $v$ | Velocity |
| $W$ | Width of the channels |
| $w$ | Width of the separating walls |
| $We$ | Weber number |
| $x$ | Thermodynamic vapor quality |
| $z$ | Flow-wise coordinate, continuous |
| $z^*$ | Fixed flow-wise location |

*Subscripts*

| | |
|---|---|
| + | Refers to the difference between the case with and without inlet orifices |
| av | Average, calculated on the geometric heated area of the channels |
| b | channel bottom, i.e. at the root of the separating walls |
| ch | Refers to channel or to the refrigerant flow along the channel |
| ch,tot | channel total, i.e. comprising channel and expansion into the outlet plenum |
| contr | Contraction |
| conv | Convective regime |
| corr | Predicted by a selected correlation, flow-wise |
| Cu | Copper |
| diff | Differential measurement over the inlet and outlet manifold |
| eq | Equivalent, i.e. using the thermophysical properties of the homogenous flow |
| exp,tp | Area expansion from channel end to outlet plenum |
| fp | At the footprint, after subtraction of heat losses of the test section |
| fr | Frictional |
| h | Hydraulic |
| hom | Mixture properties calculated with the homogeneous model |
| in | Inlet manifold |
| in,ch | Channel inlet, downstream the orifice |
| j | Generic index |
| l | Liquid |
| loc | Flow-wise, i.e. calculated along the channel at multiple location (IR camera) |
| nom | At nominal test condition |
| nucl | Nucleation regime |
| or | Orifice at the inlet of the channel |
| out | Outlet manifold |
| out,ch | Channel outlet, upstream the expansion |
| rev | Reversible |
| sat | At saturation condition |
| Si | Silicon |
| Sn | Tin |
| tp | Two-phase local, i.e. calculated at a single RTD location |
| v | Vapor |
| w | At the wall, calculated on the heated area based on fin model |
| Wall | Refers to the separating wall of the channel |
| wo | Refers to the case with inlet orifices |

the presence of nucleation in annular flows [7], the latter provoking both the enhancement of the heat transfer coefficient and the disruption of the liquid film at the walls of the channels. Among these phenomena, flow instabilities have received the greatest attention, but the triggering conditions have not been generalized yet. Nevertheless, several geometrical solutions have been investigated to mitigate the effects of vapor confinement and improve the heat transfer performance of heat sinks. For example, Hedau et al. [8] studied the impact of inlet restrictions and nano-structured walls to cope with instabilities and pressure drop fluctuations in microchannels, and concluded that both modifications could reduce the flow instabilities. In particular, nano-structures helped the re-wetting of the walls during the commencement of dryout and were more effective during the annular flow regime. On the other hand, inlet restrictions were more effective during the plug and slug flow regimes, since they limited the growth of slugs upstream. In a later study by the same authors [9], a flexible dampener was used to obtain a reduction in the flow instabilities in microchannel heat sinks. Compared to the inlet restrictions, the flexible dampener helped mitigating the instabilities with no major pressure penalty. In Al-Zaidi et al. [10,11], the effect of channel aspect ratio and heat sink material on the two-phase flow

and bubble growth characteristics was investigated. It was concluded that channels with high depth-to-width ratio can be subject to higher fluctuations, and can experience larger pressure drops and larger bubble diameters at departure - the latter being caused by stronger heating from the lateral walls. However, these fluctuations did not affect the heat transfer measurements. In their later study [11], aluminium and copper heat sinks were compared, showing that the copper heat sinks generated larger bubbles with lower departure frequencies, leading to more flow reversal and instabilities on the flow distribution. On the other hand, the aluminium heat sinks provided more nucleation sites and showed smaller bubbles being released with higher frequency.

Due to the multiplicity of phenomena occurring during boiling in confined geometries, the concept of macro-to-micro transition has been introduced in the literature to identify the conditions leading to a confined flow [12]. However no general criteria have been identified yet for it, mainly due to a missing agreement on the predominant phenomenology of this transition. In a study by Harirchian and Garimella [13] multiple channel widths and heights were compared during flow boiling to observe the triggering of bubble confinement and how it altered the heat transfer mechanism. Cross-sectional area of the flow was identified as a significant parameter driving confinement. Their study also highlighted the possibility of the coexistence of two flow patterns in the same flow section and the unsteady nature of the flow patterns, which can hinder the identification of a single heat transfer mechanism. Later investigations also showed that nucleation may be present during annular flow when high heat fluxes are applied, driving both the superposition of nucleation to convection and the onset of liquid film disruption from the heated walls [7]. As a consequence, various investigations found disagreement in the dominating heat transfer mechanisms [2]. The impact of the surface roughness and wall wettability could also play a role in defining the flow patterns and thus the heat transfer mechanisms [1]. This has promoted the use of high-speed visualization and infrared cameras to identify flow patterns and select the most appropriate prediction tools. Compared to the heat transfer, the study of pressure drops in microchannel has been object of a less extended debate and its study has been mainly focused on the identification of the best prediction methods for the frictional pressure gradients in single-tube setup. One of the challenging aspects of the study of pressure drops in microchannel heat sinks is the estimation of the pressure drops in the inlet and outlet manifold, as well as the inlet restrictions, which are often used to guarantee the absence of pressure fluctuations. A study by Huang and Thome [14] found that measured pressure drops in the outlet manifold could be as high as 51% of the overall system pressure drops and therefore the experimental assessment of these losses was recommended instead of their estimation through singe-phase fluid-dynamic methods. However, such an approach is scarce in literature. As described later in this section, investigations on pressure drops focus on a parametric analysis of the frictional pressure gradient and assess the prediction capability of existing methods, which often includes also the suitability of the homogeneous mixture model for the predictions.

### 1.1. Flow boiling of low-GWP fluids

Among the various cooling medium available for two-phase heat sinks, refrigerants represent an advantageous choice for electronics cooling [1]. However, concerns about their environmental impact and the consequent regulations [15,16] have shifted the attention of thermal experts to hydro-fluoro-olefins (HFOs) with low Global Warming Potential (GWP). In this context, R1234yf and R1234ze(E) have been identified as replacements for R134a, which is one of the most versatile refrigerant used so far. Low-GWP refrigerants were studied as drop-in alternatives in air conditioning systems [17,18]. Among the two low-GWP options, R1234yf has received more attention in flow boiling due to its use in automotive air conditioning. However, this fluid was mainly studied in single-tube setups at low heat fluxes and in channels in the millimeter range, which is very different than the conditions it would be operated in electronics cooling at high heat flux. The study of R1234ze(E) is mainly limited to single-tube studies, as reviewed in the following sections.

#### 1.1.1. Heat transfer coefficient

Saitoh et al. [19] studied the flow boiling of R1234yf in a 2 mm tube at a saturation temperature of 15°C and observed a heat transfer coefficient completely dependent on the heat flux at low vapor quality. It eventually shifted to a convection-dominated condition at high vapor quality. For their experimental conditions, the heat transfer coefficient was best predicted by the Saitoh et al. correlation [20], while the frictional pressure gradient was best predicted by the Lockhart and Martinelli correlation [21]. Del Col et al. [22] studied R1234yf in a 1 mm tube heated by a secondary fluid at a saturation temperature of 31°C, reporting a heat transfer coefficient not dependent on mass flux and dependent on vapor quality just for values below 0.3. The correlations assessed over their data under-predicted the results. Choi et al. [23] compared R1234yf with natural refrigerants in 1 mm and 3 mm tubes at saturation temperatures between 0°C and 10°C. Their heat transfer coefficient was dependent on the heat flux at low vapor quality and no effect was observed from the mass flux. Their data were used to develop a correction for the nucleate boiling suppression factor and convective enhancement factors, however their method was not verified against other data. Mancin et al. [24] studied the flow boiling of R1234yf and R1234ze(E) in an asymmetrically heated channel machined in copper at a depth of 4.6 mm. Heat flux was observed to control the heat transfer coefficient and no noticeable effects of the mass flux or the vapor quality were observed. Their data were best predicted by the Yu et al. correlation [25]. Insights on the dewetting and rewetting phenomena occurring during dryout were highlighted. Tapia and Ribatski [26] studied flow boiling of R1234yf and R1234ze(E) in a 1.1 mm tube at saturation temperature of 31°C and 41°C. Influence of both the heat and mass flux was observed on their heat transfer coefficient. Their experimental data were best predicted by Kim and Mudawar [27] as well as Kanizawa et al. [28]. Jige and Inoue [29] investigated the heat transfer coefficient of R1234yf in a 2 mm square channel. Similarly to other investigations, no effect of mass flux and vapor quality at low mass flux, while an influence was present at high vapor quality. Effects related to gravity were observed as well, possibly suggesting that no real confinement was present during this investigation. Xu et al. [30] studied the flow boiling of R134a and R1234yf in a 1.88 mm tube, comprising heat transfer, pressure drops and flow visualization. The best heat transfer predictions were given by the Bertsch et al. correlation [31] as well as the Liu and Winterton correlation [32]. Li and Hrnjak [33] investigated flow boiling of R1234ze in a 0.643 mm multiport channel, including both heat transfer analysis and visualization. Their results showed that, for this diameter, the flow was mainly plug-slug and eventually transitioned to annular flow at higher vapor quality. Flow visualization showed that during the plug flow, the flow was homogeneous and plugs were moving uniformly with the liquid. For R1234yf, no effect of the mass flux on the heat transfer coefficient was observed and the heat transfer coefficient was mainly controlled by the heat flux. In this case, the Cooper correlation [34] overpredicted the experimental values, while the Gorenflo correlation [35] could better predict the data. The best predictions were achieved with the Bertsch et al. correlation [31]. A study involving a multi-microchannel setup was the one used by Hou et al. [36], where a thermal test vehicle was built to test two-phase cooling of silicon carbide power electronics with R1234yf. By keeping the maximum chip temperature to 120°C, a footprint heat flux of 526 W/cm$^2$ was achieved in a copper heat sink. Both single- and multiple-chip arrangements were investigated, showing the general feasibility of the technique for high power-density applications. Another study by the present authors was conducted for R134a, R1234yf and R1234ze(E) in a 300 μm-wide channel to identify flow patterns and heat transfer mechanism during high heat flux flow boiling. Additional studies were concentrated on the flow boiling of other refrigerants, such

as the R1233zd or the HFE-7100. Fang et al. [37] studied the flow boiling of R1233zd(E) in minichannels with a section of (1.5 x 1.5) $mm^2$. They found that the onset of nucleate boiling depended on the mass flux and the subcooling. The best heat transfer coefficient predictions were given by Liu and Winterton [32]. Rui et al. [38] studied the performance of HFE-7100 in novel microchannel configuration: a Tesla valve microchannel heat sink and a sector bump microchannel heat sink. It was observed that the vapor structures generated in the sector bump microchannel were smaller, and this also resulted in a better heat transfer performance. The sector bump microchannel also showed lower fluctuations of the pressure drop, which were associated to the lower amount of vapor structures. Yang et al. [39] studied the flow boiling of ammonia in a diamond microchannel heat sink manufactured by laser ablation.

#### *1.1.2. Pressure drop*

To the best of the authors' knowledge, no pressure drops studies for R1234yf and R1234ze in a multi-microchannel setup are present in the literature. The studies available refer to either single-tube setups or multi-channels with high GWP refrigerants. Agostini et al. [40] studied the pressure drops in a silicon multi-microchannel evaporator and found that the pressure drops increased with the square of the mass and the heat flux. The homogeneous mixture model was recommended for their evaporator, which comprised square channels with a nominal width of 223 μm and a nominal height of 680 μm. Harirchian and Garimella [41] studied flow boiling of FC-77 for different channel geometries and found that, for a fixed heat flux, the channel pressure drops increased with the mass flux. In their measurements for a multi-channel evaporator, the pressure drops increased with heat flux as well. Huang and Thome [14] studied the flow boiling of the low-GWP refrigerant R1233zd(E). In a later study by these authors, using a database covering three refrigerants, they proposed a modified version of the Chisolm parameter [42] to predict their experimental dataset. It was also highlighted that the Kim and Mudawar model [27] was the best performing in their silicon heat sink. Al-Zaidi et al. [43] found that the method by Mishima and Hibiki [44] and the one by Keepaiboon et al. [45] were the best in predicting the channel pressure drops for their HFE-7100 in copper microchannels. In a similar experimental setup, Lee et al. [46] found that pressure drops were affected by the inlet sub-cooling and increased with the heat flux. Experimental investigations in a single tube show that the frictional pressure gradient increased with the mass flux and the vapor quality, while the impact of the heat flux was not observed. Anwar et al. [47] studied pressure drops in a vertical stainless steel tube with a diameter of 1.6 mm and found that the frictional pressure drops increased with the vapor quality and decreased with the saturation temperature. By comparing the experimental data, they observed that the homogeneous model did not return accurate predictions, while the Mishima and Hibiki correlation [44] performed reasonably. Xu et al. [30] studied the flow boiling of R134a and R1234yf in a 1.88 mm tube, and found that the best pressure drops prediction was obtained by Zhang and Webb [48] and Friedel [49] correlations. Dario et al. [50] found that the pressure drops increased with the mass flux and decreased with saturation temperature for R134a. Similarly to Anwar et al. [47], they observed that the homogeneous model was not suitable to predict the data, while the method by Mishima and Hibiki [44] was the best. Jige and Inoue [29] studied flow boiling in a 2 mm channel. They found that the pressure drops increased with the mass flux and the vapor quality. Channel shape did not influence the pressure drops and the best predictions were obtained with the Friedel [49] and Müller-Steinhagen and Heck model [51].

### *1.2. Objectives*

Despite the various solutions found to mitigate instabilities, the studies of low-GWP refrigerants in multi-microchannels are scarce and limited to relatively low heat fluxes, mostly in single-tube setups. Due to channels interaction, multi-microchannel systems present more complexities than single channels, such as flow maldistribution, premature critical heat flux and conjugate heat transfer, and they require dedicated studies. It is believed that characterizing experimentally multi-microchannels at high heat fluxes can help advancing the current knowledge on two-phase cooling of electronics to accommodate the future development of efficient thermal management systems.

The objective of this study is primarily to contribute to the body of knowledge of high heat flux flow boiling heat transfer in multi-microchannels by focusing on the scarcely investigated low-GWP refrigerants. This contribution was obtained by carrying out a parametric analysis on the flow-wise heat transfer coefficients and the channel pressure drops of R1234yf and R1234ze(E) in a multi-microchannel evaporator operated with wall heat fluxes up to 90 $W/cm^2$. Compared to the literature, the study extends the flow boiling analysis in multi-microchannel to high heat fluxes in stable flow boiling conditions, obtained by using inlet orifices. The pressure drops in the inlet orifices, as well as in the inlet and outlet manifold, were evaluated experimentally, allowing for an accurate evaluation of the channel pressure drop. The study was conducted in a multi-microchannel with a nominal width of 200 μm and nominal depth of 1200 μm, resulting in a nominal depth-to-width ratio of 6. Channels with a high depth-to-width ratio are particularly suitable to dissipate high heat loads, but have generally received less attention than the low depth-to-width counterpart. The heat transfer analysis was supported by high-speed flow visualization and the experimental results were compared to the predictions from methods published in the literature, to identify the correlations that best predict the data.

### *1.3. Outline of the study*

The paper presents briefly the experimental setup, the characteristics of the test section, and the geometrical features of the multi-microchannel evaporator. Then, the methods used for the experimental analysis of the pressure drops in the orifices, as well as in the inlet and outlet manifold, are presented. The paper continues outlining the data reduction for the heat transfer coefficient and the channel pressure drop, together with the propagated uncertainties and the experimental procedures. The results are organized as follows: concerning heat transfer, a parametric analysis of the local heat transfer coefficient, the flow-wise heat transfer coefficient, and the non-dimensional heat transfer coefficient is presented for each fluid; the results are discussed starting from an analysis based on relevant non-dimensional groups. For the pressure drop, the following contributions are outlined and discussed: the differential pressure drops over the manifold, the total channel pressure drop, the momentum pressure drops and its ratio with the manifold and channel pressure drop, and the pressure penalty introduced by the inlet orifices. Finally, the paper presents a statistical assessment of the existing prediction methods for both the flow-wise heat transfer coefficients and the channel pressure drop.

## 2. Experimental methods

This section begins by introducing the test rig and the methods used to measure the magnitude of the pressure drops in the orifices, and the inlet and outlet manifolds; then, it outlines the methods used to calculate and analyse the flow boiling heat transfer coefficient and the channel pressure drop. In particular, Section 2.1 describes briefly the experimental setup and the test section. The geometrical features of the multi-microchannels are presented in Section 2.2. Section 2.3 summarizes the experimental methods used for the evaluation of the pressure drops in the orifices and the inlet and outlet manifold. Finally, Section 2.4 describes the data reduction of the heat transfer coefficient and the channel pressure drop, the related propagated uncertainties and it outlines the experimental procedure.

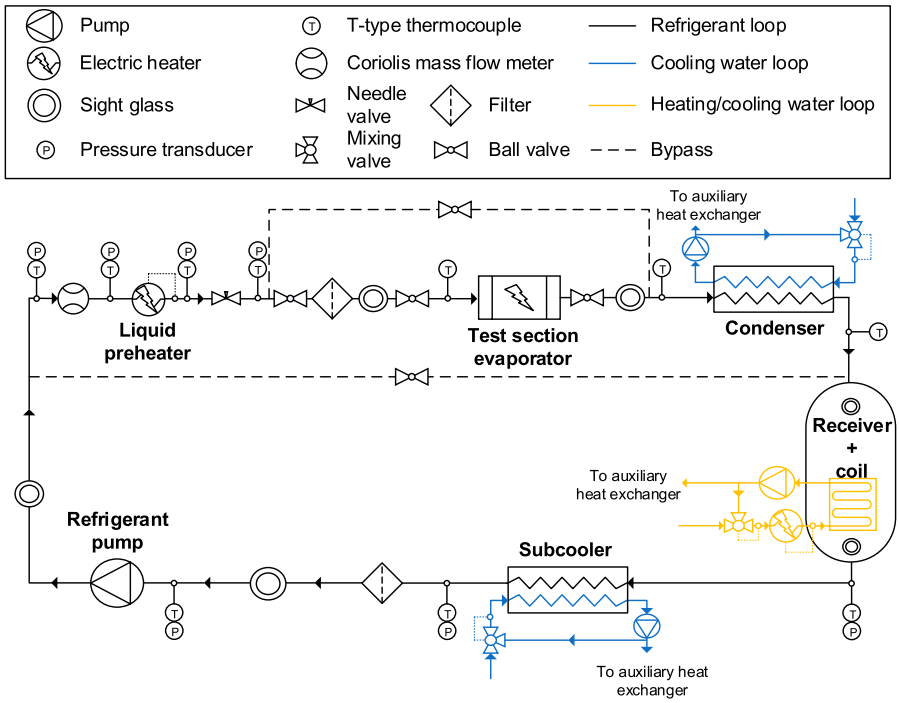


**Fig. 1.** Piping and instrumentation (P&I) diagram of the two-phase pumped loop.

### 2.1. Test rig and test section

The experimental investigation was conducted with a test rig designed and built at the Department of Mechanical Engineering of the Technical University of Denmark. The test rig was a pumped two-phase loop, where three functionally independent sections can be identified: the flow conditioning loop, the water loops and the test section. Fig. 1 shows the piping and instrumentation diagram of the test rig.

The test rig consisted of a pumped two-phase loop where a subcooled liquid flow was heated to boiling conditions in the test section. A list of the main components is reported in Table 1. The heat transfer measurements in the multi-microchannels took place in the test section, where an imposed heat flux was applied to the footprint of the channels using a custom-built microheater connected to a power supply. Temperature measurements in the form of 2-D temperature maps of the micro-heater were obtained through an infrared camera with visual access to the footprint of the multi-microchannels, where the micro-heater was vacuum-soldered. The infrared camera obtained the spatial temperature distribution over the heated area of the micro–heater. Along the centerline, the flow-wise distribution of the temperature was calculated by a width-wise average of the temperature map in a region covering 20 width-wise pixels from the centerline. The width-wise averaged temperature profile was adjusted by a constant value to match the temperature value of the two central RTDs and a moving average calculated over 15 pixels was used to remove artifacts resulting from edge effects between adjacent heating lanes. Further details on the processing of the temperature maps by the infrared camera can be found in [52]. The test section assembly is depicted in Fig. 2. The experimental setup also comprised a high-speed Complementary Metal-Oxide Semiconductor (CMOS) camera Photron Nova S9 with a 60 mm lens and a double 2 × teleconverter. The high-speed camera was mounted above the test section, thus providing visual access to the flow in the channels through a borosilicate glass mounted on the top side of the multi-microchannels. For further details on the setup, the reader may refer to the authors previous publications [52,53].

The multi-microchannels were manufactured by micro-milling in an electrolytic tough pitch copper (C101/CW004A) substrate with a Computer Numerical Control (CNC) machine. The fluid accessed the channels through an inlet plenum that comprised flow restrictions at the entrance of each channel. Likewise, the flow exited the multi-microchannels through an outlet plenum. The inlet and outlet plena were obtained by inserting micro-milled PolyEtherEtherKetone (PEEK) elements into the copper substrate, as shown in Fig. 2. Because of its low thermal conductivity ($\approx 0.25\,W/m\,K$), the PEEK inserts allowed to minimize heat dispersion to the flow in the inlet and outlet manifolds and the possibility of free bubble nucleation outside of the microchannels. The use of inlet flow orifices increased the stiffness of the flow to parallel channel instabilities and vapor backflow, thus also improving the flow distribution [54]. The orifices were characterized by a flow area reduction of 65%. The high-speed visualization confirmed that the restrictions effectively avoided vapor backflow in the inlet plenum and minimized parallel channel instability, as no periodic oscillations in the pressure drops signal were observed during the investigation. The entire test section was insulated with polyurethane foam. The assembly of the multi-microchannels in the test section is depicted in Fig. 3. Uncertainties of the measuring instruments are reported in Table 2.

### 2.2. Multi-microchannel geometry

The microchannels used for the investigation were obtained by milling the copper baseplate using a cutting tool with a nominal width of 200 μm. 25 parallel microchannels with a nominal depth of 1200 μm and nominal length of 1 cm were obtained. The dimensions of the manufactured microchannels were evaluated using a confocal microscope Lext OLS4000 by Olympus. The measured height and width were, respectively, 1167 μm and 198 μm, resulting in an hydraulic diameter $D_h$ of 338 μm (±25 μm). Overall, the microchannels had a heated area of 6.33 $mm^2$ and a flow area of 5.78 $mm^2$. Using a high magnification lens, the surface roughness resulting from milling the channels was measured on dedicated specimens using the same feed rate, cutting depth, and material for the test microchannels. The average roughness of the lateral sides of the channels was 360 nm. This value was in agreement with Young et al. [55], who presented roughness values for machining of copper.

**Table 1**
Main components and instruments of the test rig.

| Component | Model |
|---|---|
| Pump | Tuthill D-series gear pump |
| Pump inverter | Danfoss VLT FC300 |
| Thermocouples | Omega K- 0.25 mm and T- type 0.5 mm |
| Flow meter | Micro Motion Coriolis CMFS010M |
| Infrared camera | FLIR a655sc + 50 μm close-up lens |
| High speed camera | Photron Nova S9 + 60 mm lens + 2 × 2x teleconverters |
| Power supply TS | Keysight N5770A |
| Microheater TS | Custom made platinum serpentine |
| RTDs | Custom made, integrated into the microheater |
| Pressure sensor | Danfoss AKS33 |
| Differential pressure sensor | Endress-Hauser Deltabar PMD75 |
| Data acquisition | National Instruments CompactDAQ + Labview |

**Table 2**
Instrument type and expanded uncertainties.

| Instrument | $u$ | Units | Range |
|---|---|---|---|
| Thermocouples, T-type | ±0.15 | °C | 18–50 |
| Thermocouples, K-type | ±0.16 | °C | 18–50 |
| RTDs | ±0.09 | °C | 25-160 |
| Low pressure transmitter | ±0.025 | bar | 0–10 |
| High pressure transmitter | ±0.04 | bar | 0–21 |
| Mass flow meter | ±0.1% | kg/hr | 5–55 |
| Power supply, voltage | ±0.1% + 0.15 | V | 0–150 |
| Power supply, current | ±0.1% + 0.03 | A | 0–10 |

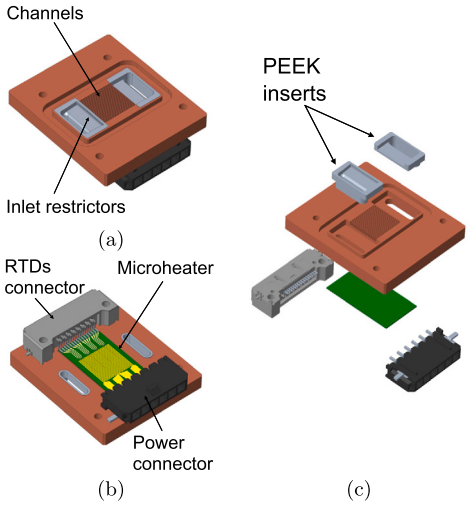


**Fig. 2.** Top view (a), bottom view (b) and exploded view (c) of the multi-microchannels.

### 2.3. Evaluation of manifolds and orifice pressure drop

Since the pressure measurements on the test section were directly obtained right upstream the inlet plenum and right downstream the outlet one, the pressure drops in the manifolds, $\Delta p_{in}$, and the orifice, $\Delta p_{or}$, were both necessary to calculate the pressure at the inlet of the microchannels, $p_{in,ch}$. An illustration of the pressure drops contribution to the test section is shown in Fig. 4. To calculate the channel outlet pressure, $p_{out,ch}$, the pressure drops of the two-phase flow expanding from the channel to the outlet plenum, $\Delta p_{exp,tp}$, and the pressure drops in the outlet manifold, $\Delta p_{out}$, were used. The channel inlet pressure, $p_{in,ch}$, and outlet pressure, $p_{out,ch}$, were calculated according to Eqs. (1) and (2), respectively,

$$p_{in,ch} = p_{in} - \Delta p_{in} - \Delta p_{or} \tag{1}$$

$$p_{out,ch} = p_{out} + \Delta p_{out} + \Delta p_{ex,tp} \tag{2}$$

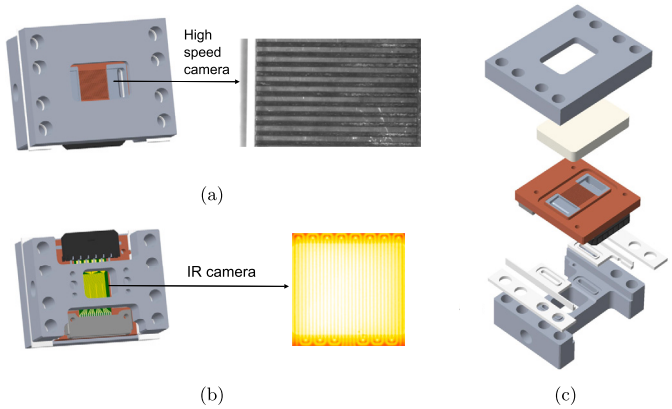


**Fig. 3.** Visual access of the high-speed camera to the top of the multi-microchannels (a), visual access of the infrared camera to the bottom of the multi-microchannels (b), test section assembly (c).

The pressure drops of the outlet manifold, $\Delta p_{out}$, inlet manifold, $\Delta p_{in}$, and the orifice, $\Delta p_{or}$, were evaluated experimentally with the aid of a dedicated baseplate with identical manifolds to the standard test baseplate, but without channels, as shown in Fig. 5a. The dedicated baseplate was mounted in a test section with a metallic top cover with a pressure tap at its center. This pressure tap was used to make differential pressure measurements for the inlet and outlet manifold. The central pressure tap is shown in Fig. 5b.

#### 2.3.1. Single-phase pressure drops in the inlet manifold

To measure the single-phase pressure drops in the inlet manifold, the differential pressure transducer was connected to the inlet manifold pressure tap and the central pressure tap in the top cover of the dedicated test section. In this way, neglecting the frictional losses in the straight passage of the copper baseplate, the measured pressure drops corresponded to the inlet manifold pressure drop. Single-phase measurements were done with the three refrigerants R1234yf, R1234ze(E) and R134a at laboratory conditions. The liquid pressure drops factor in the inlet manifold, $f_{in}$, was fitted with respect to the Reynolds number, $Re$, calculated at the largest section of the manifold, as shown in Eq. (3). The R-square of the fit for $Re < 7000$ was 0.899, and the RMSE was 4.95.

$$f_{in}(Re) = \frac{\Delta p_{in}}{\frac{1}{2}\rho_{l,in} v_{l,in}^2} = \begin{cases} 2.35 \cdot 10^8 Re^{-2.03} & \text{if } Re < 7000 \\ 3.96 & \text{if } Re > 7000 \end{cases} \tag{3}$$

where $\rho_{l,in}$ and $v_{l,in}^2$ indicate, respectively, the density of the liquid in the inlet manifold and the velocity of the flow at the largest section of the inlet manifold.

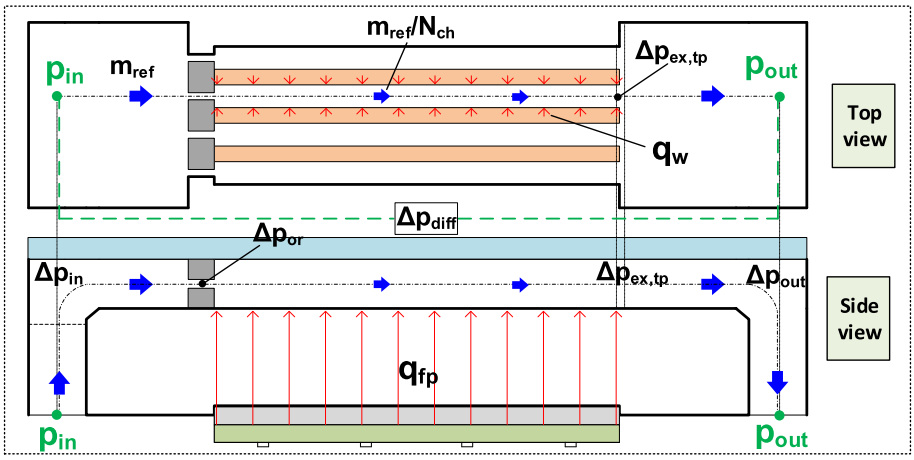


**Fig. 4.** Illustration of the pressure drops contributions in the test section, top view and side view.

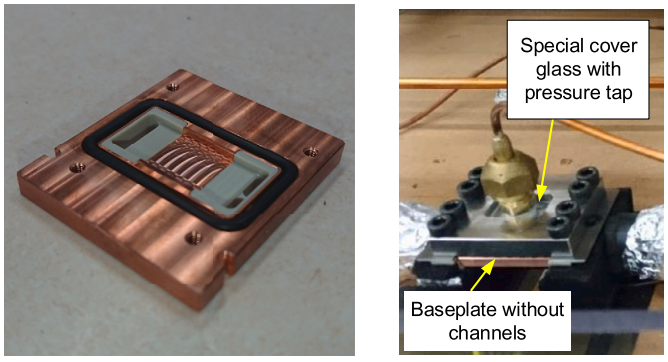


**Fig. 5.** Image of the dedicated baseplate without channels (a) and test section with the baseplate mounted together with the cover glass with a central pressure tap (b).

### 2.3.2. Two-phase pressure drops in the outlet manifold

To measure the two-phase pressure drops in the outlet manifold, the differential pressure transducer was connected to the central pressure tap in the top cover and the outlet manifold pressure tap. In this case, the preheater was used as the heat source to modulate the vapor quality entering and exiting the test section during the pressure drops measurements. Two-phase pressure drops measurements were done with the three refrigerants R1234yf, R1234ze(E) and R134a at laboratory conditions, for a wide range of vapor quality and mass flow rates. The ratio, denoted with $R$, between two-phase pressure drops in the outlet manifolds, $\Delta p_{out}$, and the dynamic pressure of the liquid-only flow, $\frac{1}{2}\rho_l v_l^2$, in the largest section of the outlet manifold was fitted with respect to the Weber number based on the homogeneous mixture properties, $We_{hom}$, and the outlet vapor quality, $x_{out}$, for each of the refrigerant, as shown in Eqs. (4) and (5).

$$R(We_{hom}) = \frac{\Delta p_{out}}{\frac{1}{2}\rho_l v_l^2} = (45.87 We_{hom}^{-0.023} x_{out}^{1.11}) \quad \text{for} \quad \text{R1234yf} \tag{4}$$

$$R(We_{hom}) = \frac{\Delta p_{out}}{\frac{1}{2}\rho_l v_l^2} = (564.2 We_{hom}^{-0.29} x_{out}^{1.04}) \quad \text{for} \quad \text{R1234ze} \tag{5}$$

The R-square of the fit was 0.994 and the RMSE was 0.843 for R1234yf. For R1234ze(E), the R-square was 0.993 and the RMSE was 2.36. This kind of fit was preferred to the two-phase liquid multiplier approach because it provided the lowest error.

### 2.3.3. Pressure drops in the inlet orifices

The pressure drops over the orifice, $\Delta p_{or}$, was obtained by comparing the overall pressure drops in the standard test section with and without the inlet orifice at the same refrigerant mass flow rate. In the former case, PEEK inserts without inlet restrictions were used. For the case without orifices, the pressure difference measured over the test section in adiabatic conditions and single-phase flow, $\Delta p_{diff}$, was given by Eq. (6),

$$\Delta p_{diff} = \Delta p_{in} + (\Delta p_{contr,fr} + \Delta p_{contr,rev}) + \Delta p_{ch} + \Delta p_{exp} + \Delta p_{out} \tag{6}$$

where the pressure drops due to the expansion of the single phase flow into the outlet plenum was denoted by $\Delta p_{exp}$. For convenience, the pressure drops over the contraction in Eq. (6) has been divided into the reversible ($\Delta p_{contr,rev}$) and the frictional ($\Delta p_{contr,fr}$) contributions. When the orifices were present, the measured pressure drop, $\Delta p_{diff,wo}$, corresponded to Eq. (7),

$$\Delta p_{diff,wo} = \Delta p_{in} + \Delta p_{or,rev} + \Delta p_{or,fr} + \Delta p_{ch} + \Delta p_{exp} + \Delta p_{out} \tag{7}$$

Assuming $\Delta p_{or,rev} = \Delta p_{contr,rev}$, the difference in pressure drops in single-phase between the case with and without orifice is shown in Eq. (8),

$$\Delta p_{diff,wo} - \Delta p_{diff} = \Delta p_{or,fr} - \Delta p_{contr,fr} \tag{8}$$

By rearranging the terms in Eq. (8) and isolating the frictional pressure drops in the orifice, the equation can be rewritten as in Eq. (9),

$$\Delta p_{or,fr} = (\Delta p_{diff,wo} - \Delta p_{diff}) + \Delta p_{contr,fr} \text{ where } (\Delta p_{diff,wo} - \Delta p_{diff}) = \Delta P_+ \tag{9}$$

It is shown that $\Delta p_{or,fr}$ can be obtained by the experimental value $\Delta P_+$ and $\Delta p_{contr,fr}$ at different mass flow rates. $\Delta p_{contr,fr}$ was calculated according to Chalfi and Ghiaasiaan [56] and the values of $\Delta P_+$ were regressed with respect to the dynamic pressure in the orifice $\frac{1}{2}\rho_l v_{or}^2$. The final formula for the calculation of the orifice pressure drops $\Delta p_{or,fr}$ was Eq. (10),

$$\Delta p_{or,fr} = f_{or} \frac{1}{2}\rho_l v_{or}^2 + \Delta p_{contr,fr} \tag{10}$$

where $f_{or}$ was a regression constant dependent on the fluid. The values of the constants were 1.25 and 1.39 for R1234yf and R1234ze(E), respectively. The fit of the experimental data versus the constant for the orifice friction factor is shown in Fig. 6.

## 2.4. Data reduction

### 2.4.1. Pressure drop

The total pressure drops in the channel including the expansion losses in the outlet plenum, $\Delta p_{ch,tot}$, was calculated as shown in Eq. (11),

$$\Delta p_{ch,tot} = p_{in,ch} - p_{out,ch} \text{ where } \begin{cases} p_{in,ch} = p_{in} - \Delta p_{in} - \Delta p_{or} \\ p_{out,ch} = p_{out} + \Delta p_{out} \end{cases} \quad (11)$$

where $\Delta p_{in}$, $\Delta p_{out}$ and $\Delta p_{or,fr}$ were calculated according to Section 2.3. The sum of the momentum and frictional pressure drops contribution in the channel, $\Delta p_{tp,tot}$, was calculated as in Eq. (12),

$$\Delta p_{tp,tot} = \Delta p_{ch,tot} - \Delta p_{exp,tp} \quad (12)$$

Pressure drops for the liquid-vapor mixture at the expansion from the channel to the outlet plenum, $\Delta p_{exp,tp}$, were obtained by summing the frictional pressure drops and the reversible one. The frictional contribution was calculated through the friction factor as presented in [56], while the momentum contribution was calculated using the homogeneous mixture model for the reversible pressure drops in the expansion as shown in Eq. (13),

$$\Delta p_{exp,tp} = f_{exp,fr} \frac{\rho_{hom} v^2_{ch,hom}}{2} + \frac{\rho_{hom}(v^2_{ch,hom} - v^2_{out,hom})}{2} \quad (13)$$

The calculated channel pressure drop, $\Delta p_{tp,tot}$, corresponded to the sum of the frictional and the momentum change pressure drops of the evaporating flow in the channels only. The momentum change pressure drop, $\Delta p_{mom}$, was estimated by calculating the mass flux $G$ and the homogeneous void fraction at the outlet ($\epsilon_{out}$) and inlet ($\epsilon_{in}$) of the channels as shown in Eq. (14),

$$\Delta p_{mom} = G^2 \{ [\frac{x^2_{out}}{\rho_v \epsilon_{out}} + \frac{1 - x^2_{out}}{\rho_l (1 - \epsilon_{out})}] - [\frac{x^2_{in}}{\rho_v \epsilon_{in}} + \frac{1 - x^2_{in}}{\rho_l (1 - \epsilon_{in})}] \} \quad (14)$$

since the inlet conditions of the flow were sub-cooled, both the inlet vapor quality and the inlet void fraction were considered null in Eq. (14).

### 2.4.2. Heat transfer coefficient

The data reduction of the heat transfer coefficient for the current setup was described in detail in a previous work of the authors [52]. A short summary is reported here for convenience of the reader. The inlet and outlet channel pressure calculated in Eq. (11) were linearly interpolated along the channel length to calculate the pressure profile of the flow along the channel. Since the channels were short, a linear interpolation was considered appropriate for the study. The linear pressure profile was combined with an energy balance along the channel to calculate the temperature profile in the sub-cooled region and the vapor quality profile in the two-phase region. The temperature profile in the two-phase region was calculated from the pressure profile according to the saturation condition as shown in Eqs. (15)-(18),

$$p_{ch}(z) = p_{in,ch} - \frac{p_{in,ch} - p_{out,ch}}{L_{ch}} z \quad (15)$$

$$i_{ch}(z) = i(p_{in,ch}, T_{in,ch}) + \frac{\dot{Q}}{\dot{m}} \frac{z}{L_{ch}} \quad (16)$$

$$x_{loc}(z) = \frac{i_{ch}(z) - i_{sat}(p_{ch}(z))}{i_{fg}(p_{ch}(z))} \quad (17)$$

$$T_{ch}(z) = \begin{cases} T_{sat}(p_{ch}(z)) & \text{if } x(z) > 0 \\ T(p_{ch}(z), i_{ch}(z)) & \text{if } x(z) < 0 \end{cases} \quad (18)$$

where $z$ denotes the continuous axial coordinate along the channel length, $\dot{Q}$ is the total heat rate absorbed by the flow and $L$ is the channel length. For the heat transfer analysis, two heat transfer coefficients were calculated: a flow-wise heat transfer coefficients, $h_{loc}(\tilde{z})$, and a two-phase local heat transfer coefficient, $h_{tp}$. Using the discrete temperatures at the bottom of the channels, $T_b(\tilde{z})$, the separating walls were approximated to fins to calculate the heat transfer coefficient. The flow-wise heat transfer coefficients, $h_{loc}(\tilde{z})$, were calculated as defined in Eqs. (19)-(22) [10,13,54],

$$h_{loc}(\tilde{z}) = \frac{q_w(\tilde{z})}{T_b(\tilde{z}) - T_{ch}(\tilde{z})} \quad (19)$$

$$q_w(\tilde{z}) = \frac{q_{fp} \cdot (W + W_{wall})}{W + 2H\eta(\tilde{z})} \quad (20)$$

$$\eta(\tilde{z}) = \frac{\tanh(m(\tilde{z})H)}{m(\tilde{z})H_{ch}} \quad (21)$$

$$m(\tilde{z}) = \sqrt{\frac{2h_{loc}(\tilde{z})}{k_{Cu} W_{wall}}} \quad (22)$$

where $h_{loc}(\tilde{z})$ was the flow-wise heat transfer coefficient at 24 discrete flow-wise locations $\tilde{z}$ along the channels, $q_w(\tilde{z})$ was the wall heat flux and $H_{ch}$ was the channel depth. The two-phase local heat transfer coefficient, $h_{tp}$, at the location $\tilde{z} = z^*$ of an RTD located at 0.125 cm from the channel outlet, was calculated as given in Eq. (23),

$$h_{tp} = \frac{q_w(\tilde{z} = z^*)}{(T^*_b - T(\tilde{z} = z^*))} \quad (23)$$

where $T^*_b$ was the temperature at the bottom of the channel and it was defined as in Eq. (24),

$$T^*_b = T_{RTD} - \Delta T_{Si} - \Delta T_{Sn} - \Delta T_{Cu} \quad (24)$$

where the terms $T_{RTD}$, $\Delta T_{Si}$, $\Delta T_{Sn}$, and $\Delta T_{Cu}$ denote the temperature measurement of the RTD and the temperature drop in the silicon microchip, the layer of tin and the copper substrate under the channels. The temperature drops in the silicon, tin and copper layers were calculated by a one-dimensional conduction model. The two-phase local heat transfer coefficient was used to study the effect of the heat and mass flux on the local two-phase heat transfer coefficient, while the flow-wise heat transfer coefficient was used to highlight the effect of the flow-wise vapor quality and the heat flux on the heat transfer. To discriminate quantitatively between the heat transfer mechanisms occurring in the channel, a heat transfer analysis based on non-dimensional group was conducted. The non-dimensional analysis was based on the Boiling Number ($Bo$), Convection Number ($Co$), Confinement Number ($N_{Conf}$), Weber Number ($We(\tilde{z})$), and the two-phase heat transfer enhancement factor ($\psi(\tilde{z})$) as given in Eqs. (25)-(30),

$$Bo = \frac{q_{av}}{G\Delta i} \quad (25)$$

$$We(\tilde{z}) = \frac{G^2 D_h}{\rho_l(\tilde{z})\sigma} \quad (26)$$

$$Co(\tilde{z}) = [\frac{1}{x_{loc}(\tilde{z})} - 1]^{0.8} (\frac{\rho_v}{\rho_l})^{0.5} \quad (27)$$

$$N_{Conf} = \frac{1}{D_h} [\frac{\sigma}{g(\rho_l - \rho_v)}]^{0.5} \quad (28)$$

$$Bi(\tilde{z}) = \frac{h_{eq}(\tilde{z}) H^2_{ch}}{w_{wall} k_{Cu}} \quad (29)$$

$$\psi(\tilde{z}) = \frac{h_{loc}(\tilde{z})}{h_l} \quad (30)$$

where $q_{av}$ was the average heat flux over the heated area of the channels, i.e. it did not depend on the fin efficiency, and $h_{eq}(\tilde{z})$ was the heat transfer coefficient calculated using the Dittus-Boelter equation [57] with the thermophysical properties of the homogeneous two-phase flow and $h_l$ was the heat transfer coefficient calculated by the Dittus-Boelter [57] as if only the liquid was flowing in the channels. Even if most of the operating conditions fall into the transition to turbulence regime, the use of a correlation for the liquid heat transfer coefficient based on a method for turbulent flow is preferred, as both the presence of the orifice, the short length of the channels and the boiling could promote strong mixing in the liquid phase.

## 2.5. Analysis of the uncertainties

Error propagation analysis was performed on the data reduction. Propagated errors were calculated as in [58] and doubled to expand the confidence level. The input uncertainty was calculated as the square root of the sum of the squared standard deviation of the measured quantity and the square of the systematic error. Since the channels were small and the heat fluxes were high, the channel dimensional

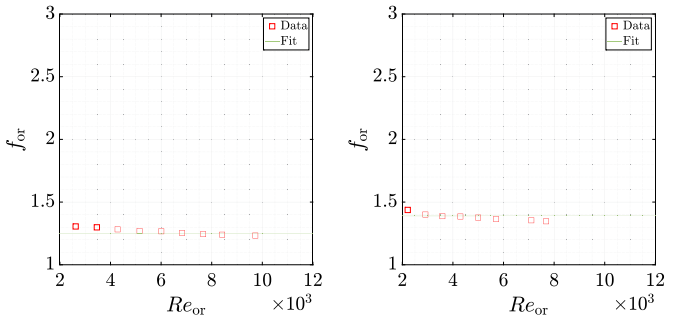


(a) $f_{or} = 1.25 \pm 0.05$ (b) $f_{or} = 1.39 \pm 0.03$

**Fig. 6.** Trends of $f_{or}$ for (a) R1234yf and (b) R1234ze(E).

uncertainty was the major source of uncertainty in the heat transfer coefficient. The second highest contribution came from the uncertainty in the wall superheat, which was related to the uncertainties of the RTDs used to zero-adjust the IR temperature profile. For the entire experimental database, the average uncertainty and its standard deviation for the $h_{tp}$ were 22.3% ± 5.7%, while for the wall heat flux, $q_w$, they were 5.75% ± 1.4%; the local thermodynamic vapor quality, $x_{loc}$, had an average uncertainty and a standard deviation of 5.2% ± 4%.

The total pressure drops in the channel had an overall average uncertainty and a standard deviation of 12.5% ± 7.7% for the measurements with an outlet vapor quality above 0.05. The uncertainty was highest at outlet vapor quality close to zero and lowest at the highest outlet vapor quality, when the pressure drops in the channel was the largest. The uncertainty in the channel pressure drops was mainly dependent on the uncertainty of the channel width, the orifice friction factor and the channel expansion friction factor. On average, for the whole dataset, these three variables accounted for a share of 4%, 60% and 20% of the entire uncertainty budget.

### 2.6. Experimental procedure and test conditions

The experimental procedures are summarized by the flow diagram reported in Fig. 7 and described here in brief for the convenience of the reader.

Each test was characterized by three experimental conditions: the mass flux, $G$, the outlet saturation temperature, $T_{out,ch}$, and the outlet vapor quality, $x_{out}$. The outlet vapor quality was varied by increasing the heat dissipation at the microheater soldered at the bottom of the heat sink. The heat dissipation ranged from low heat fluxes, i.e., values above boiling incipience, to the critical heat flux (CHF). The CHF was achieved for outlet vapor qualities in the range 0.4 - 0.9, the highest value of CHF being obtained for a nominal mass flux of 1140 kg/m$^2$ s and the lowest for a nominal mass flux of 418 kg/m$^2$ s. The signals from the sensors were recorded when the thermocouple signals' moving average changed less than 0.05°C over two minutes. The dissipated heat flux was increased at each step to obtain a thermodynamic quality variation at the outlet of 0.05–0.07, until the occurrence of the CHF, which resulted in a very steep wall temperature increase with time. An example of such a steep temperature rise is shown in a previous paper by the authors [59]. Labview recordings were taken for 120 s, and their average values were used for the data reduction procedures. Temperatures and pressure signals were logged at a frequency of 10 Hz. When an experimental series was started, the inlet sub-cooling was set to a nominal value of 4 ± 1°C. Due to slow thermal response of the preheater, the inlet subcooling was controlled with an accuracy of ± 1°C, with higher values obtained at the higher heat fluxes. Throughout this work, a distinction is made between the *nominal* test conditions, which are used to describe the conditions in the plots, and the *effective* ones, which are reported in the plot of each experimental series. The objective of the experimental campaign was to obtain local heat transfer coefficients of the

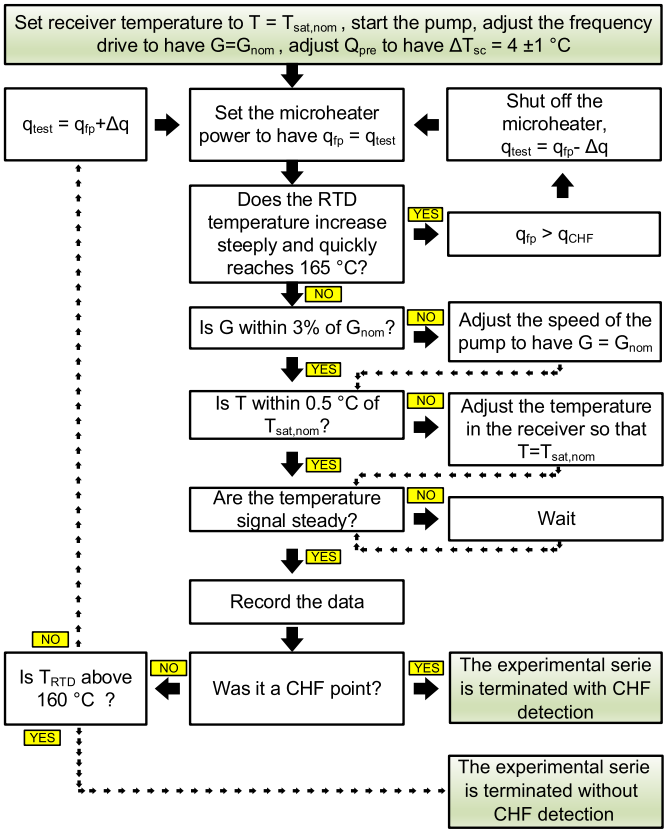


**Fig. 7.** Flow diagram of the experimental procedure followed to get an experimental series at a prescribed $G_{nom}$ and $T_{sat,nom}$.

multi-microchannels for a wide range of experimental conditions. For each fluid, a parametric analysis was conducted with respect to four nominal mass fluxes, $G_{nom}$, (416, 622, 909 and 1139 kg/m$^2$ s) and two nominal outlet saturation temperatures, $T_{sat,nom}$, (30.5°C and 40.5°C). The resulting variation of the fin efficiency was between 0.68 and 0.92, while the resulting variation of the non-dimensional groups was the following: $0.0006 < Bo < 0.0109$, $1.99 < N_{Conf} < 2.56$, $790 < Re_l < 2714$ and $6.24 < We_l < 75.61$.

## 3. Results and discussion

In Section 3.1 the results are presented as the two-phase local heat transfer coefficient ($h_{tp}$) versus the wall heat flux ($q_w$) and the flow-wise heat transfer coefficient ($h_{loc}$) versus the flow-wise vapor quality ($x_{loc}$). A regression of the results with the non-dimensional groups in Eqs. (25)-(30) was used to analyse the dominating heat transfer modes. Then, in Section 3.2, the pressure drops results are presented as differential value over both the manifold and the channel, i.e. after the orifice and before the expansion in the outlet plenum. The relative magnitude of the momentum change pressure drops and the pressure penalty introduced by the orifice is highlighted. Finally, Section 3.3 is dedicated to the comparison of the results with the predictions of existing correlations. The comparison of the heat transfer coefficient was performed using the method presented in [52] to account for the asymmetric heating conditions in the channels. Each subsection of the results is discussed independently.

### 3.1. Two-phase local heat transfer coefficient

Fig. 10a and Fig. 11a show the two-phase local heat transfer coefficient for R1234yf and R1234ze(E) for a nominal saturation temperature of 30.5°C and four mass fluxes. The experimental data are divided into

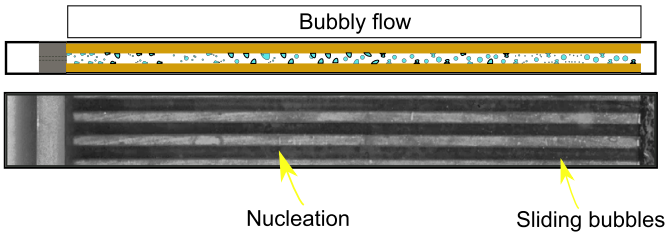


**Fig. 8.** High-speed image and schematic illustration of the flow of R1234yf in the channels for a mass flux of 416 kg/m$^2$ s and a wall heat flux of 8 W/cm$^2$. Boiling regime I.

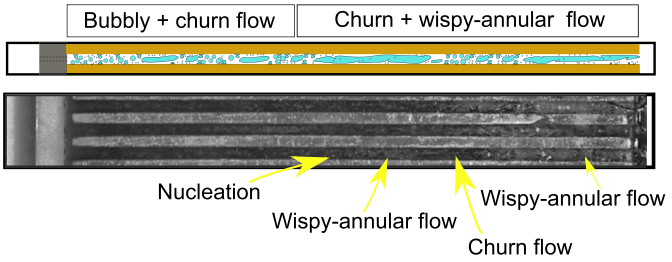


**Fig. 9.** High-speed image and schematic illustration of the flow of R1234yf in the channels for a mass flux of 416 kg/m$^2$ s and a wall heat flux of 51 W/cm$^2$. Boiling regime II.

three boiling regimes according to how the heat transfer coefficient changes with the heat and the mass flux. For boiling regime I, the mass flux does not affect significantly the heat transfer coefficient and the heat flux drives the heat transfer coefficient, which corresponds to a nucleation-dominated regime. In boiling regime II, the local heat transfer coefficient changes with the channel mass flux and the heat flux. In boiling regime III, the heat transfer coefficient decreased steeply with the applied heat flux as a result of dryout inception and progression. High speed visualization of this boiling regime for 300 μm-wide channels was described in detail in [52].

Referring to the boiling regime I, Fig. 10a shows that, for a heat flux of 15 W/cm$^2$, the local heat transfer coefficient was, respectively, 20.3 kW/m$^2$K and 18.7 kW/m$^2$K for a mass flux of 416 kg/m$^2$ s and 1138 kg/m$^2$ s. A similar variation occurred for R1234ze, as shown in Fig. 11a. To discriminate the dominance of nucleation, the experimental growth rate of the heat transfer coefficient with the heat flux was compared with the exponent predicted by the Gorenflo correlation [35]. This is indicated by the blue line in Figs. 10a-11a. The presence of nucleation was also confirmed by the high-speed visualization. An high-speed image of the flow for a mass flux 416 kg/m$^2$ s and a wall heat flux of 8 W/cm$^2$ for R1234yf is shown in Fig. 8. For the boiling regime II, which occurred at heat fluxes in the range 30 W/cm$^2$ to 80 W/cm$^2$ for R1234yf and 40 W/cm$^2$ to 100 W/cm$^2$ for R1234ze(E), increasing the mass flux from 416 kg/m$^2$ s to 1138 kg/m$^2$ s corresponded to a variation in the heat transfer coefficient from 31 kW/m$^2$K to 40 kW/m$^2$K at a heat flux of 55 W/cm$^2$, for R1234yf. During this regime, the growth rate of the heat transfer coefficient with the heat flux departed from the nucleation-dominated condition. For this boiling regime, an unstable wispy-annular flow was observed in the channels. An high-speed image of the flow for a mass flux 416 kg/m$^2$ s and a wall heat flux of 54 W/cm$^2$ for R1234yf is shown in Fig. 9. During boiling regime III, the heat transfer coefficient decreased with the heat flux due to intermittent dewetting of the channel walls.

The flow-wise heat transfer coefficients are shown in Fig. 10b for R1234yf at mass flux of 416 kg/m$^2$ s. For a wall heat flux lower than 54 W/cm$^2$, the plot shows firstly a uniform heat transfer coefficient, which then increases with the local vapor quality. A similar trend is observed for R1234ze(E) in Fig. 11b. The plot also shows that, as the local vapor quality grows, the heat transfer coefficient curves tend to collapse into a single one as long as dryout does not take place. The independence of the flow-wise heat transfer coefficient with the heat flux and the collapse of the curves as the vapor quality grows can be associated to a convection-dominated condition. A dryout condition is indicated by dashed curves, which show an almost monotonic decrease of the flow-wise heat transfer coefficient with the flow-wise vapor quality.

To discriminate the nucleation-dominated and the convection-dominate region in a quantitative way, further insights into the heat transfer data were outlined by non-dimensionalization of the heat transfer coefficients with the groups presented in Eqs. (25)-(30). Fig. 10c shows the non-dimensional heat transfer coefficient of R1234yf with respect to the $Co$ for measurements before dryout inception. Fig. 11c displays the same for R1234ze(E). Both figures display how the curves are characterized by two regions: a region of almost horizontal curves for Co >> 1 and a decreasing region for Co << 1. The resulting plot is similar to the one originally developed for macro-channels [60], with which the current data show a qualitative agreement in trend.

Due to the reduced channel size, the impact of the $N_{\mathrm{Conf}}$ was highlighted by regressing the experimental data with the non-dimensional groups presented in Eqs. (25)-(30). To extend the range of the $N_{\mathrm{Conf}}$, the current dataset has been combined with the data for a 300 μm-wide channels obtained in a previous study [52]. The comparison between the two geometries can be observed in Fig. 12b for a nominal mass flux of 415 kg/m$^2$ s. To identify how the non-dimensional groups controlled the two heat transfer regimes, data with Co > 4 were regressed for the nucleation-dominated regime while data with Co < 1 were regressed for the convection-dominated regione. The first subset of data with Co > 4 was regressed by Eq. (31),

$$\psi_{\mathrm{nucl}} = c_0 Bo^{c_1} We^{c_2} N_{\mathrm{Conf}}^{c_3} Bi^{c_4} \tag{31}$$

returning the following constants: $c_0 = 52.15$, $c_1 = 0.565$, $c_2 = 0.058$, $c_3 = 0.098$ and $c_4 = -0.458$. The second subset of data with Co < 1 was regressed by Eq. (32),

$$\psi_{\mathrm{conv}} = c_5 Co^{c_6} We^{c_7} N_{\mathrm{Conf}}^{c_8} Bi^{c_9} \tag{32}$$

returning the following constants: $c_5 = 30.477$, $c_6 = -0.43$, $c_7 = -0.18$, $c_8 = -1.003$ and $c_9 = -0.065$. A final regression function for the full experimental range of $Co$ was built as shown in Eq. (33),

$$\psi = max(\psi_{\mathrm{conv}}, \psi_{\mathrm{nucl}}) \tag{33}$$

Fig. 13 shows an example of how the regression captured the experimental data for the lowest mass flux tested. The power fit returned a MRSE of 1.42 for the experimental points with $Co < 1$ and MRSE of 0.92 for the points with $Co > 4$. As outlined in Fig. 13, the non-dimensional heat transfer coefficient trends were captured well by the selected non-dimensional groups. The regression highlighted that the $Bo$ dominated the heat transfer performance with a growth exponent of 0.565 for the high $Co$ range, while the $We$ was almost irrelevant and having an exponent of 0.058. This agrees with what was observed in the analysis of the boiling regime I. On the other hand, moving to lower $Co$ range, the non-dimensional heat transfer coefficient grew inversely with the $Co$ with an exponent of -0.43. The significance of the $We$ increased in magnitude but still remained comparably small. Notably, both the bubble confinement number $N_{\mathrm{Conf}}$ and the equivalent $Bi$ changed significantly their importance as the flow transitioned from a high $Co$ to a low $Co$. The regression suggested that the confinement $N_{\mathrm{Conf}}$ influenced significantly the heat transfer behavior of the flow in the convective-dominated region, while the same occurred for the equivalent $Bi$ in the high $Co$ region.

To complete the analysis, the impact of the saturation temperature on the local heat transfer coefficient was assessed by conducting experiments at a nominal saturation temperature of 40.5°C. The results can be observed in Fig. 12a for R1234yf at a nominal mass fluxes of 908 kg/m$^2$ s and 415 kg/m$^2$ s. Both R1234yf and R1234ze showed an increase of the local heat transfer coefficient with the saturation tem-

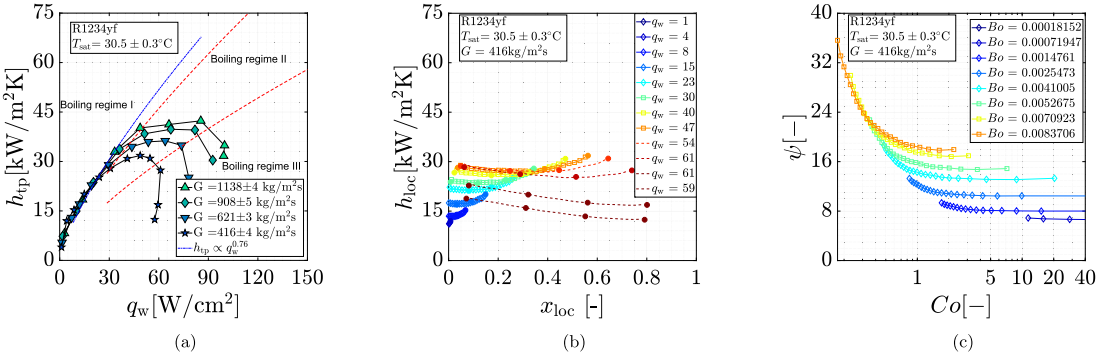


**Fig. 10.** Heat transfer trends of R1234yf (a) Two-phase local heat transfer coefficient versus the wall heat flux in W/cm$^2$ at the outermost RTD (z = 0.88 cm), (b) flow-wise heat transfer coefficient (c) non-dimensional flow-wise heat transfer coefficient. (For interpretation of the colors in the figure(s), the reader is referred to the web version of this article.)

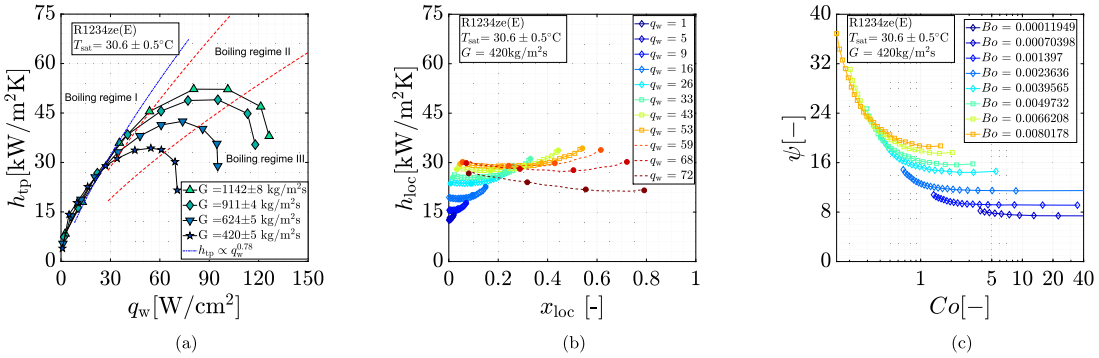


**Fig. 11.** Heat transfer trends of R1234ze (a) Two-phase local heat transfer coefficient versus the wall heat flux in W/cm$^2$ at the outermost RTD (z = 0.88 cm), (b) flow-wise heat transfer coefficient, (c) non-dimensional flow-wise heat transfer coefficient.

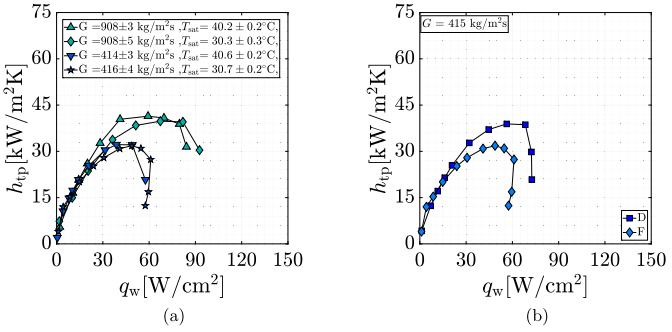


**Fig. 12.** Comparison of the two-phase local heat transfer coefficient of R1234yf versus the wall heat flux at the outermost RTD (z = 0.88 cm) for (a) nominal saturation temperature of 30.5°C and 40.5°C, (b) for channel width of 200 μm and 300 μm, labeled, respectively, with F and D in the plot.

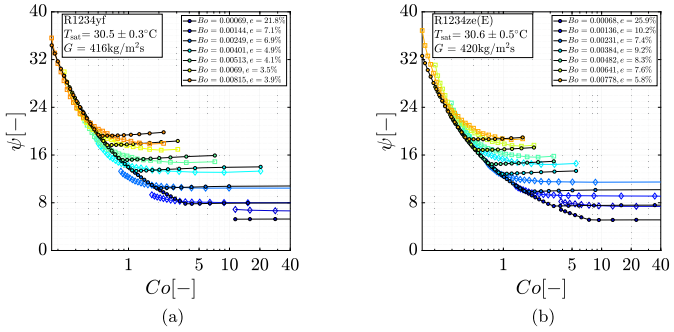


**Fig. 13.** Non-dimensional flow-wise heat transfer coefficient and its prediction by the applied power fit in Equation 33 (black lines) for (a) R1234yf and (b) R1234ze(E) at a mass flux of 418 kg/m$^2$ s.

perature at the lower heat fluxes, while the onset of the dryout regime was anticipated with increasing saturation temperature. This behavior was in agreement with the transition from a heat flux dominated regime to a convection-dominated regime.

### 3.1.1. Discussion of heat transfer

The experimental data show that the heat transfer coefficient evolved following three main boiling regimes when the applied wall heat fluxes ranged from low to near-critical values. The first boiling regime is associated to the dominance of bubble nucleation in the heat transfer process: this was confirmed both by the growth rate of the heat transfer coefficient with the heat flux and by the visual inspection through the high-speed camera, an example of which is shown in Fig. 8. This condition occurred in the lower range of heat flux tested and finds agreement with studies on single tubes performed at low heat fluxes and larger diameters [22,47]. In spite of the relatively high $N_{Conf}$, there is a quite evident demarcation of the nucleation-dominated condition from the convection-dominated one as shown in Fig. 10c and 11c. In the convection-dominated regime, the presence of an unstable wispy-annular flow, as confirmed by the high-speed image in Fig. 9, drives the heat transfer performance. Non-dimensionalized results for both the 200 μm and 300 μm channels were regressed with respect to relevant non-dimensional groups, in particular the $N_{Conf}$, and the equivalent *Bi*, which accounted for the impact of the separating wall thickness on the heat diffusion through the lateral walls - this was deemed to be relevant due to the high aspect ratio of the channels and the slender fins. The analysis through the regression of non-dimensional groups showed that, for large *Co*, the *Bo* and the equivalent *Bi* drove the heat transfer, as indicated by the magnitude of the power exponents in Equation (31). While the dominance of the *Bo* agrees with the qualitative behavior of flow boiling in macrochannels according to conventional theories

[3], it is notable that the wall $Bi$ was the second most important factor in the heat transfer performance. Since this number is associated to the heat diffusion in the separating wall by its definition, the wall thickness can play a significant role in the overall heat transfer performance. This is due to the asymmetric heating condition which evaporators for electronics cooling experience. Lower equivalent $Bi$ may be associated to a more uniform heat diffusion in the separating walls and, possibly, more nucleation sites activated at high $Co$. Since it is related to the temperature uniformity along the height of the separating walls, the equivalent $Bi$ is directly related to the efficiency of the wall in activating nucleation sites. However, high-speed images do not allow to distinguish the number of active nucleation sites due to shades and reflections in the very narrow and deep channels. Very slender walls could lead to a poor heat flux diffusion and generate a situation in which the heat flux applied at the channel footprint remains confined to the bottom of the channels, possibly resulting in lower heat transfer coefficient at the entire channel section. It is interesting to note that from the regression, at high $Co$, the impact of the bubble confinement is actually weaker than the equivalent $Bi$, i.e. than the heat flux confinement. In fact, the exponent of the $N_{\mathrm{Conf}}$ is about one fifth of the equivalent $Bi$. The situation is completely reversed when a convection-dominated region at low $Co$ is considered. In this condition, the $Co$ and the $N_{\mathrm{Conf}}$ drove the heat transfer performance. Here the exponent of $N_{\mathrm{Conf}}$ becomes around ten times the one of the equivalent $Bi$. It is believed that the dominance of the $N_{\mathrm{Conf}}$ arises from the instability of the wispy-annular flow, which is driven by the confinement of the high-inertia vapor phase into the microchannels, which has been identified a trigger of two-phase instabilities as explained in Section 1. According to the regressions, the higher the confinement, the more deleterious is the instability of the flow for the heat transfer. Moreover, high $N_{\mathrm{Conf}}$ implies that surface tension forces take more importance. On the other hand, the lower surface tension, the higher the wettability. Hence, high confinement may result in a lower wettability of the walls by the liquid. In this situation, the impact of the $Bi$ on the heat transfer coefficient is limited, as the convection at the walls drives the heat transfer performance and not the nucleation. Limited heat diffusion in the walls may be a significant effect for microchannel heat sinks, which operate with asymmetric heating and tend to have slender separating walls. Since the literature is missing an experimental study investigating this parameter, further investigations are recommended in this direction.

### 3.2. Two-phase channel pressure drops

Figs. 14a and 15a show the manifold pressure drops for R1234yf and R1234ze(E) at a nominal saturation temperature of 30.5°C and four mass fluxes. The figures show that for both fluids the total channel pressure drops increased with the wall heat flux and the mass flux. It is interesting to note that, at high heat flux, the rate of change of manifold pressure drops with the wall heat flux is higher than at lower heat flux. As an example for R1234yf at low heat flux, increasing the wall heat flux from 10.5 W/cm$^2$ to 20.7 W/cm$^2$ increased the pressure drops from 5.1 kPa to 6.6 kPa for a mass flux of 908 kg/m$^2$ s. Conducting the same analysis starting at a heat flux of 66.8 W/cm$^2$ and increasing to 82.1 W/cm$^2$, the pressure drops went from 13.4 kPa to 16.6 kPa. By making reference to the heat transfer coefficients in Fig. 10a - 11a, showing that the heat transfer coefficient is decreasing, this steeper increase in the pressure drops can be associated with the dryout occurring in the channels. The general increase of the pressure drops in the manifold is driven by the increase in the mean velocity of the flow, which is proportional to the mass flux and the heat flux, affecting the mean vapor quality.

The total channel pressure drops $\Delta p_{\mathrm{tp,tot}}$ and the momentum pressure drops $\Delta p_{\mathrm{mom}}$ are displayed in Fig. 14b-15b and Fig. 14c-15c, respectively. For both fluids, these pressure drops are mainly increasing with the heat flux but are not influenced significantly by the mass flux. As an example, for a wall heat flux of 65 W/cm$^2$, the sum of the frictional and momentum pressure drops is 10.7 kPa, 10.4 kPa and 10.7 kPa for mass fluxes of 1138 kg/m$^2$ s, 908 kg/m$^2$ s and 621 kg/m$^2$ s, respectively. This behavior is associated to two counteracting effect taking place when the mass flux was increased at a fixed heat flux. On one hand, the momentum pressure drops in the channel increased, as displayed in Figs. 14c and 15c; on the other hand, the mean vapor quality decreased and this may lead to a reduction of the frictional component of the pressure drop. It is interesting to note that, as displayed in Fig. 14d-14e for R1234yf and Fig. 15d-15e for R1234ze(E), the momentum pressure drops calculated with an homogeneous model for the void fraction accounts for around 30% to 60% of the manifold pressure drops and for around 60% to 130% of the total channel pressure drop. A share above 100% is possible due to the pressure recovery at the outlet of the channel, which occurs due to the expansion in the outlet plenum. The importance of the momentum pressure drops in the overall pressure change of the flow is significant. Compared to low heat fluxes applications, this condition occurs because of the high heat fluxes involved (i.e. relatively high change in momentum of the flow) and the short channel length (i.e. relatively low frictional pressure drop). Finally, Fig. 14f and 15f display the ratio of the orifice pressure drops and the total channel pressure drop, i.e. the pressure penalty introduced by the orifices. It is observed that the magnitude of the pressure penalty increases with the mass flux and decreases with the heat flux. This penalty can range from 20% to 500%, depending on the operating conditions.

The impact of the saturation temperature on the manifold pressure drops for R1234yf can be observed in Fig. 16a for nominal mass fluxes of 415 kg/m$^2$ s and 908 kg/m$^2$ s. Both R1234yf and R1234ze(E) showed a decrease of the channel pressure drops with the saturation temperature, mainly in the higher heat flux range. This can be associated to the reduced viscosity of the refrigerants and the lower shearing effect of the vapor over the liquid as the density difference reduces with higher saturation temperatures. Fig. 16c shows the pressure drops for a mass flux of 415 kg/m$^2$ s in the 200 μm and 300 μm channels. The larger diameters show lower pressure drops and they both increase with the heat flux. The difference between the two geometries is mainly associated to the different mean vapor qualities in the channel, driving different momentum pressure drop.

#### 3.2.1. Discussion of pressure drop

The effect of the mass flux and heat flux on the manifold pressure drops results obtained for the two fluids is in agreement with other studies performed at lower heat fluxes in multi-microchannels [40,61,62]. The impact of the saturation temperature has not been highlighted before in multi-channels and most data available belong to single channel studies. We observed that there is an agreement with single channel studies [47] considering the impact of the saturation temperature. These impacts are mainly related to the reduction in dynamic viscosity. However, the observed effect was minor. A possible explanation to this is that the frictional pressure drops contribution is almost negligible in the current setup. This is also corroborated by the fact that, calculating the momentum pressure drops with the homogeneous void fraction - the homogeneous model was proven to be a suitable approach to microchannel geometries in a study by Ribatski et al. [63] - the estimate covers a very large share of the total channel pressure drop, as indicated in Fig. 14d and 15d. This has indeed profound consequences on the driving factors of the pressure drop, being principally the mass flux and the outlet vapor quality as these influence the momentum pressure drop. By considering the pressure penalty introduced by the orifice, this study shows that for systems operating at high heat fluxes, the overall pressure drops are dominated by the orifice and the momentum change, relating the pumping power needed for the system to two main contributions.

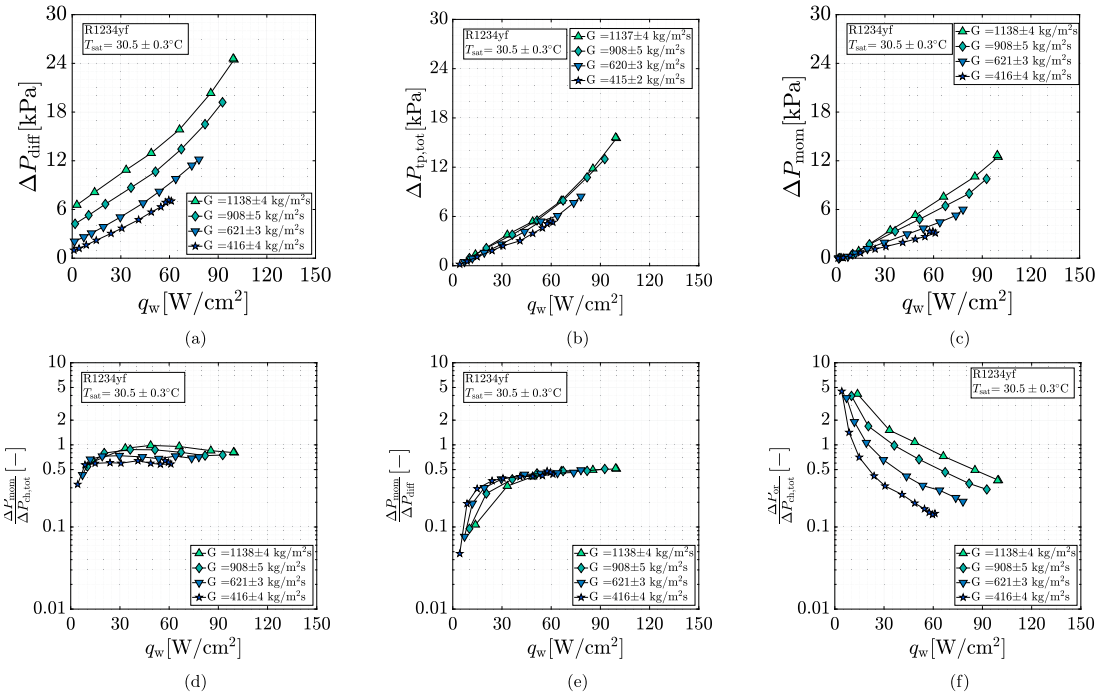


**Fig. 14.** Pressure drops data for R1234yf (a) differential pressure drops over the manifold, $\Delta P_{diff}$, (b) channel pressure drops $\Delta P_{tp,tot}$, (c) channel momentum pressure drops $\Delta P_{mom}$, (d) ratio between momentum pressure drops and total channel pressure drops, $\Delta P_{ch,tot}$, (e) ratio between momentum pressure drops and manifold pressure drops, $\Delta P_{diff}$, (f) ratio between orifice pressure drops and total channel pressure drops, $\Delta P_{ch,tot}$.

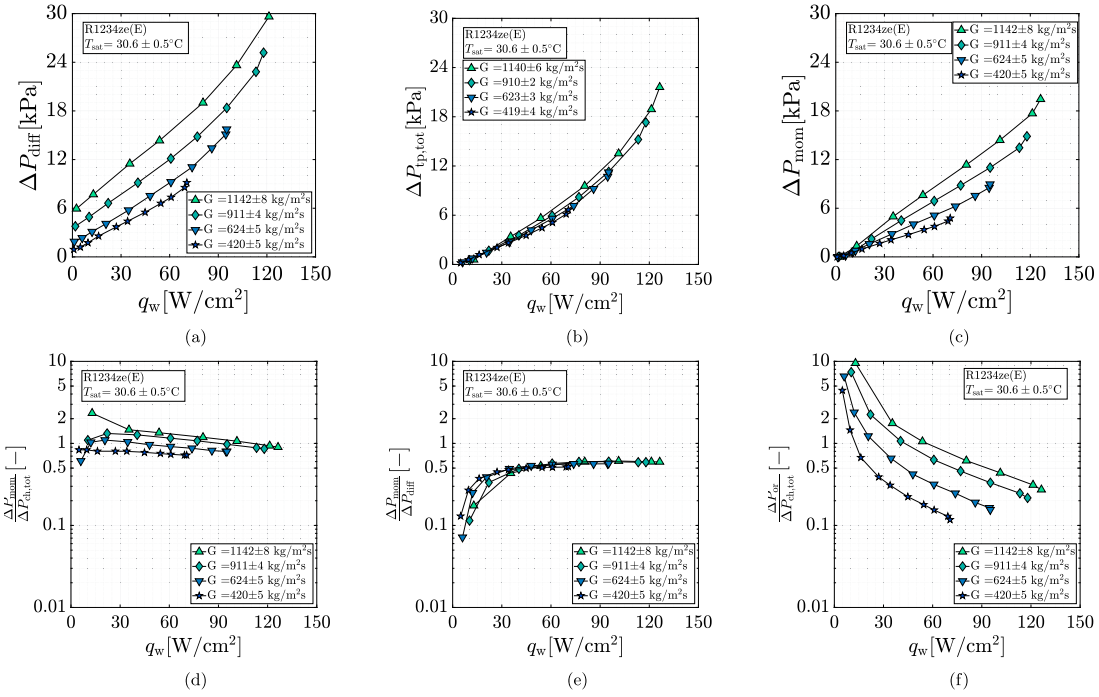


**Fig. 15.** Pressure drops data for R1234ze, (a) differential pressure drops over the manifold, $\Delta P_{diff}$, (b) channel pressure drops $\Delta P_{tp,tot}$, (c) channel momentum pressure drops $\Delta P_{mom}$, (d) ratio between momentum pressure drops and total channel pressure drop, $\Delta P_{ch,tot}$, (e) ratio between momentum pressure drops and manifold pressure drop, $\Delta P_{diff}$, (f) ratio between orifice pressure drops and total channel pressure drop, $\Delta P_{ch,tot}$.

### 3.3. Comparison with correlations

The experimental data of the present study, both heat transfer coefficient and pressure drop, were compared to the predictions of literature correlations. For the flow-wise heat transfer coefficients, general correlations based on the superposition of nucleate and convective boiling were employed. In particular, the correlations by Bertsch et al. [31], Mahmoud and Karayiannis [64] and by Kandlikar [65] were used, since they were developed for microchannels and both combined the effect of nucleation-dominated behavior and the convection-dominated one. Together with these, also the Cooper correlation [34], specifically developed for nucleate boiling, was also considered for the assessment to highlight the impact of neglecting convection effects and boiling suppression. Only local values referring to a saturated condition and for

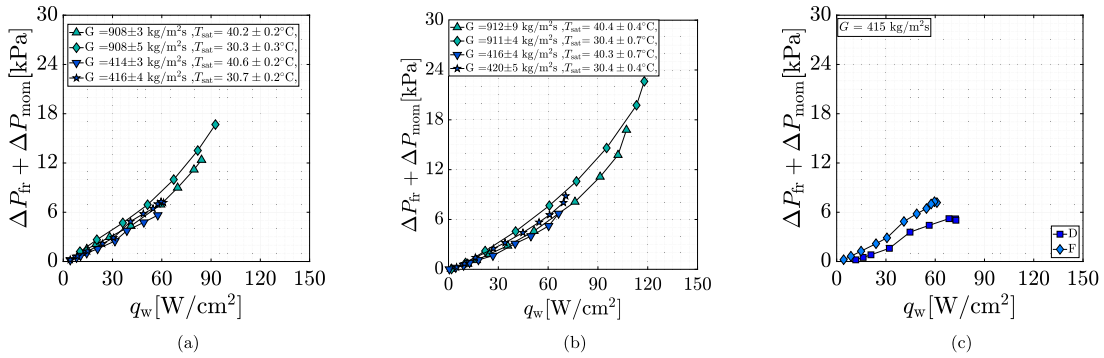


**Fig. 16.** Comparison of the two-phase pressure drops versus the wall heat flux for (a) nominal saturation temperature of 30.5°C and 40.5°C for R1234yf, (b) nominal saturation temperature of 30.5°C and 40.5°C for R1234ze(E), (c) nominal channel width of 200 μm and 300 μm, labeled, respectively, with F and D in the plot, for R1234yf.

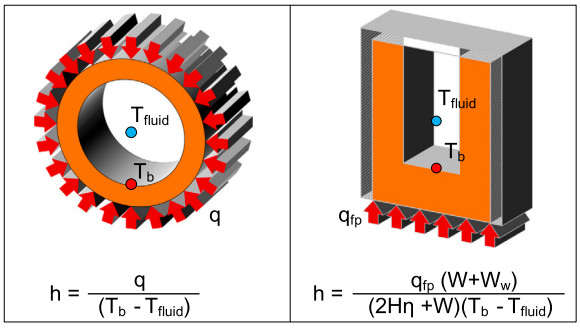


**Fig. 17.** Illustration of the physical distribution of the heat flux (red arrows) in the section of a round pipe uniformly heated (left) and in the section of a single high aspect ratio channel heated from below, typical of heat sinks (right).

measurements belonging to boiling regime I and II were considered for the comparison. These measurements were selected based on a threshold value of the standard deviation for the outermost RTD of 0.014 Ω. Since most of the correlations were developed for uniformly heated single tubes, the methodology presented in Criscuolo et al. [52] was used to account for asymmetric heating conditions taking place in the heat sinks. An illustration of the physical situation described by the correlation and the one corresponding to this study is reported in the sketch in Fig. 17.

For the channel pressure drop, the frictional components was calculated with the methods by Chisholm [42] and Müller-Steinhagen and Heck [51], since these methods were often regarded as suitable in predicting experimental results in previous studies on single tubes, as presented in Section 1.1.2. Moreover, the method by Huang and Thome [62] and Kim and Mudawar [66] were also considered as they were specifically developed for multi-microchannel setups. The momentum pressure drops in the channel was calculated by calculating the void fraction through the homogeneous mixture model.

The resulting parity plots are shown in Fig. 18 for the flow-wise heat transfer coefficients and in Fig. 19 for the channel pressure drop. The statistical assessment of the correlations is reported in Table 3 and Table 4. The assessment showed that the correlations that best predicted the heat transfer coefficient were those by Bertsch et al. [31] and Mahmoud and Karayiannis [64]. It is noteworthy to observe that, from the parity plots, all the correlations systematically over-predicted the experimental data for large values of the flow-wise heat transfer coefficients. Due to the increasing heat fluxes, the correlations were predicting a higher heat transfer coefficients, but these increases were not measured. This is indeed connected with the presence of dominant convective effects and the intermittent behavior of the flow, as highlighted in the analysis of the experimental results in Section 3.1. Regarding the pressure drop, the best methods to predict the data were the one from Huang and Thome [62] and Müller-Steinhagen and Heck [51]. It is noteworthy that, except for the Kim and Mudawar [66], the pressure drops correlations gave relatively fair results. This could be a consequence of the fact that the frictional pressure drops have a minor influence compared to the momentum pressure drop. The main takeaway from the comparisons, therefore, is that calculating the momentum pressure drops through the homogeneous void fraction could return fair results for the test conditions considered.

**Table 3**
Statistical evaluation of the local heat transfer coefficient predictions by literature correlations.

| | MAPE | MPE | SD | $\%_{30\%}$ |
|---|---|---|---|---|
| Bertsch et al. [31] | 20.1% | -0.04% | 25.7% | 78.1% |
| Karayannis and Mahmoud [67] | 24.5% | 8.1% | 32.7% | 73.5% |
| Cooper [34] | 25.7% | 3.5% | 35.1% | 66.4% |
| Kandlikar [65] | 33.9% | -9.8% | 40.5% | 46.4% |
| Kim and Mudawar [68] | 147% | 147% | 115% | 6.9% |

**Table 4**
Statistical evaluation of the pressure drop predictions by literature correlations.

| | MAPE | MPE | SD | $\%_{30\%}$ |
|---|---|---|---|---|
| Huang and Thome [62] | 22.2% | 22.2% | 19.2% | 72.1% |
| Müller-Steinhagen and Heck [51] | 22.8% | 22.8% | 19.4% | 71.4% |
| Chisolm [42] | 27% | 27% | 27.7% | 72.8% |
| Kim and Mudawar [66] | 72.2% | 72.2% | 49.6% | 25.8% |

## 4. Conclusion

This study presented an experimental investigation on the heat transfer coefficient and pressure drops of two low-GWP refrigerant fluids, R1234yf and R1234ze(E), during flow boiling under high heat flux conditions, up to 90 W/cm$^2$ at the wall. The study was conducted in a multi-microchannel evaporator heated at its base by a microheater chip. The magnitude of the applied heat flux spanned from a boiling incipience level to the critical heat flux conditions, thus providing a complete picture of how the heat transfer and pressure evolve in the possible heat flux range. The impact of heat and mass flux on the flow-wise heat transfer coefficient was analyzed and the effect of the relevant non-dimensional groups was assessed with a regression analysis of the results. The two-phase pressure drops in the channels was evaluated by deducting the experimental pressure drops in the inlet manifold, outlet manifold, and the inlet orifices from the differential pressure measurements over the test section. A dedicated test section was built to measure the pressure drops in the manifold and orifices. Finally, the experimental flow-wise heat transfer coefficient and the channel pressure

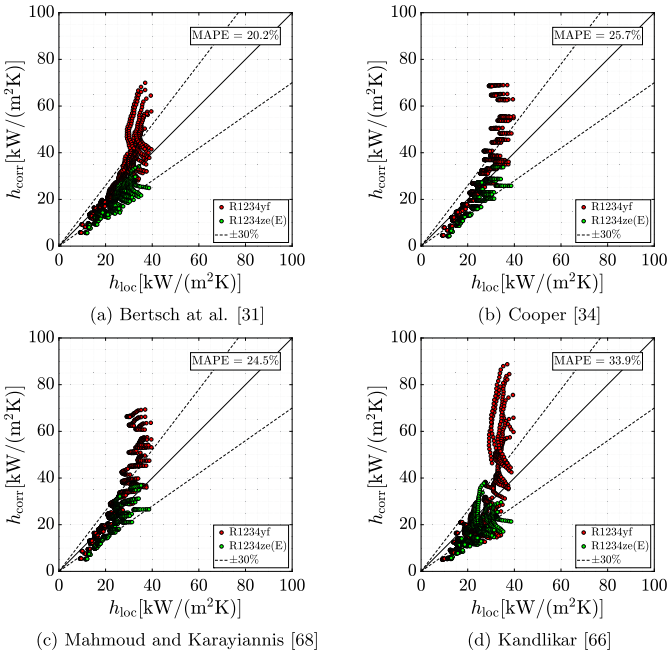


(a) Bertsch at al. [31] (b) Cooper [34]

(c) Mahmoud and Karayiannis [68] (d) Kandlikar [66]

**Fig. 18.** Parity plot of correlations employed for the comparison with the experimental data.

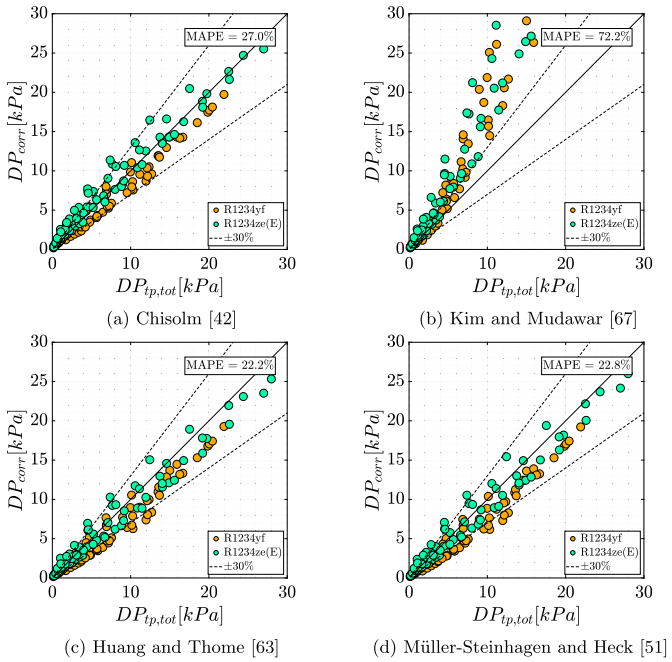


(a) Chisolm [42] (b) Kim and Mudawar [67]

(c) Huang and Thome [63] (d) Müller-Steinhagen and Heck [51]

**Fig. 19.** Parity plot of correlations employed for the comparison with the experimental data.

drops were compared to predictions from the literature. The findings of the study can be summarized as follows:

- During flow boiling in the multi-microchannel evaporator, the local heat transfer coefficient transitioned from a heat-flux-dominated condition to a mixed mass- and heat-flux-dominated one. Dryout eventually occurred in the channels leading to the decrease of the heat transfer coefficient until the critical heat flux was achieved. Despite the relatively high confinement number $N_{\mathrm{Conf}}$, in the heat-flux-dominated conditions, the heat transfer coefficient increased with the wall heat flux at a rate very similar to the predictions by Gorenflo [35] for nucleate boiling. As the heat flux at the wall was increased, the effect of the mass flux and a deviation from the nucleation-dominated region was eventually observed. This was due to the intermittent establishment of a wispy-annular flow. Compared to the 300 μm wide channels, the local heat transfer coefficient was lower in the convection-dominated region.
- The heat transfer results were analyzed in a non-dimensional analysis. The non-dimensional heat transfer trends agreed well with macrochannel models, showing a transition from a flat nucleation-dominated region to a steep convection-dominated one. Since the $N_{\mathrm{Conf}}$ was larger than 1, the results were combined with those obtained for a 300 μm wide channel and regressed to identify the impact of the $N_{\mathrm{Conf}}$ and the equivalent wall $Bi$. By this approach, it was observed that the $N_{\mathrm{Conf}}$ had an important role for the convection-dominated region, in particular through its impact on the flow instabilities. On the other hand, for the nucleation-dominated condition, the heat transfer was influenced by the $Bo$ and the wall $Bi$, which was interpreted an indicator of the confinement of the heat flux to the bottom of the channels in case of asymmetrical heating. This approach also showed that the $We$ did not influence significantly the heat transfer performance. Since evaporators for electronics cooling are in most cases only heated from one side, a further insight into the impact of the separating walls on the heat transfer coefficient is recommended for the future.
- The study showed that the pressure drops over the test section increased with the mass flux and the wall heat flux, as both contributed to increase the mean velocity of the flow. However, the evaluation of the channel pressure drops showed that, along the channels, the pressure drops were changing weakly with the mass flux and were mainly dependent on the heat flux. This effect was attributed to two counteracting effects: as the mass flux was increased at a fixed heat flux, the momentum pressure drops increases and the vapor quality decreases. By evaluating the momentum pressure drops through the homogeneous void fraction, it was observed that, for this kind of setup operating at high heat fluxes, the relative magnitude of the momentum pressure drops compared to the channel and the manifold pressure drops can range from 60% to 130%. This indicated that, as devices are operated at high heat fluxes, the estimation of the momentum pressure drops becomes the most important to evaluate the pumping power.
- The flow-wise heat transfer coefficient and the two-phase channel pressure drops were compared against correlations available in the literature. The correlations by Bertsch et al. [31] and Mahmoud and Karayiannis [64] performed the best, with a MAPE of 20.2% and 24.5%, respectively. The two-phase channel pressure drops was best predicted by the methods by Huang and Thome [62] for the frictional pressure drop, combined with the momentum pressure drops calculated using the void fraction based on the homogeneous mixture model. It is noteworthy that, for short channels at high heat flux like in this study, the momentum change dominated the channel pressure drops and, therefore, the most influencing factor for the prediction of the pressure change was related to how accurately the momentum pressure drops could be estimated.

## Declaration of competing interest

The authors declare that they have no known competing financial interests or personal relationships that could have appeared to influence the work reported in this paper.

## Data availability

Data will be made available on request.

## References


[1] T.G. Karayiannis, M.M. Mahmoud, Flow boiling in microchannels: fundamentals and applications, Appl. Therm. Eng. 115 (2017) 1372–1397.
[2] L. Cheng, G. Xia, Fundamental issues, mechanisms and models of flow boiling heat transfer in microscale channels, Int. J. Heat Mass Transf. 108 (2017) 97–127.
[3] M.M. Shah, Chart correlation for saturated boiling heat transfer: equations and further study, ASHRAE Trans. 88 (1982).
[4] S. Kandlikar, A general correlation for saturated two-phase flow boiling heat transfer inside horizontal and vertical tubes, J. Heat Transf.- Trans. ASME 112 (1990) 219–228.
[5] J.R. Thome, L. Consolini, Mechanisms of boiling in micro-channels: critical assessment, Heat Transf. Eng. 31 (2010) 288–297.
[6] L.E. O'Neill, I. Mudawar, Review of two-phase flow instabilities in macro- and microchannel systems, Int. J. Heat Mass Transf. 157 (2020) 119738.
[7] N. Borhani, B. Agostini, J.R. Thome, A novel time strip flow visualisation technique for investigation of intermittent dewetting and dryout in elongated bubble flow in a microchannel evaporator, Int. J. Heat Mass Transf. 53 (2010) 4809–4818.
[8] G. Hedau, P. Dey, R. Raj, S.K. Saha, Combined effect of inlet restrictor and nanostructure on two-phase flow performance of parallel microchannel heat sinks, Int. J. Therm. Sci. 153 (2020).
[9] G. Hedau, R. Raj, S.K. Saha, Complete suppression of flow boing instability in microchannel heat sinks using a combination of inlet restrictor and flexible dampener, Int. J. Heat Mass Transf. 182 (2022).
[10] A.H. Al-Zaidi, M.M. Mahmoud, T.G. Karayiannis, Effect of aspect ratio on flow boiling characteristics in microchannels, Int. J. Heat Mass Transf. 164 (2021).
[11] A.H. Al-Zaidi, M.M. Mahmoud, T.G. Karayiannis, Flow boiling in copper and aluminium microchannels, Int. J. Heat Mass Transf. 194 (2022).
[12] J.R. Thome, Boiling in microchannels: a review of experiment and theory, Int. J. Heat Fluid Flow 25 (2004) 128–139.
[13] T. Harirchian, S.V. Garimella, The critical role of channel cross-sectional area in microchannel flow boiling heat transfer, Int. J. Multiph. Flow 35 (2009) 904–913.
[14] H. Huang, N. Borhani, J.R. Thome, Experimental investigation on flow boiling pressure drop and heat transfer of R1233zd(E) in a multi-microchannel evaporator, Int. J. Heat Mass Transf. 98 (2016) 596–610.
[15] M. Schulz, D. Kourkoulas, European regulation no 517/2014 of the European Parliament and of the council of 16 April 2014 on fluorinated greenhouse gases and repealing regulation (ec) no 842/2006, J. Eur. Union 2014 (2014) L150.
[16] U. Nations, Amendment to the Montreal protocol on substances that deplete the ozone layer XXVII, Kigali 2016.
[17] A. Mota-Babiloni, J. Navarro-Esbrí, Á. Barragán, F. Molés, B. Peris, Drop-in energy performance evaluation of R1234yf and R1234ze(E) in a vapor compression system as R134a replacements, Appl. Therm. Eng. 71 (2014) 259–265.
[18] L.P.M. Colombo, A. Lucchini, L. Molinaroli, Experimental analysis of the use of R1234yf and R1234ze (E) as drop-in alternatives of R134a in a water-to-water heat pump, Int. J. Refrig. 115 (2020) 18–27.
[19] S. Saitoh, C. Dang, Y. Nakamura, E. Hihara, Boiling heat transfer of HFO-1234yf flowing in a smooth small-diameter horizontal tube, Int. J. Refrig. 34 (2011) 1846–1853.
[20] S. Saitoh, H. Daiguji, E. Hihara, Correlation for boiling heat transfer of r-134a in horizontal tubes including effect of tube diameter, Int. J. Heat Mass Transf. 50 (2007) 5215–5225.
[21] R. Lockhart, R. Martinelli, Proposed correlation of data lor isothermal two-phase, two-component flow in pipes, Chem. Eng. Prog. 45 (1949).
[22] D. Del Col, S. Bortolin, D. Torresin, A. Cavallini, Flow boiling of R1234yf in a 1 mm diameter channel, Int. J. Refrig. 36 (2013) 353–362.
[23] K.I. Choi, J.T. Oh, K. Saito, J.S. Jeong, Comparison of heat transfer coefficient during evaporation of natural refrigerants and R-1234yf in horizontal small tube, Int. J. Refrig. 41 (2014) 210–218.
[24] S. Mancin, A. Diani, L. Rossetto, Flow boiling heat transfer, dewetting-rewetting, and dryout visualization of HFOs in an asymmetrically heated rectangular plain channel, Appl. Therm. Eng. 107 (2016) 960–974.
[25] J. Yu, S. Momoki, S. Koyama, Experimental study of surface effect on flow boiling heat transfer in horizontal smooth tubes, Int. J. Heat Mass Transf. 42 (1999) 1909–1918.
[26] D.F. Sempértegui-Tapia, G. Ribatski, Flow boiling heat transfer of R134a and low GWP refrigerants in a horizontal micro-scale channel, Int. J. Heat Mass Transf. 108 (2017) 2417–2432.
[27] S.M. Kim, I. Mudawar, Review of databases and predictive methods for heat transfer in condensing and boiling mini/micro-channel flows, Int. J. Heat Mass Transf. 77 (2014) 627–652.
[28] F.T. Kanizawa, C.B. Tibiriçá, G. Ribatski, Heat transfer during convective boiling inside microchannels, Int. J. Heat Mass Transf. 93 (2016) 566–583.
[29] D. Jige, N. Inoue, Boiling heat transfer, pressure drop, and flow pattern in a horizontal square minichannel, Int. J. Heat Fluid Flow 78 (2019) 108433.
[30] Y. Xu, Z. Yan, L. Li, Flow boiling heat transfer, pressure drop and flow patterns of the environmentally friendly refrigerant R1234yf for cooling avionics, Appl. Therm. Eng. 209 (2022).
[31] S.S. Bertsch, E.A. Groll, S.V. Garimella, A composite heat transfer correlation for saturated flow boiling in small channels, Int. J. Heat Mass Transf. 52 (2009) 2110–2118.
[32] Z. Liu, R. Winterton, A general correlation for saturated and subcooled flow boiling in tubes and annuli, based on a nucleate pool boiling equation, Int. J. Heat Mass Transf. 34 (1991) 2759–2766.
[33] H. Li, P. Hrnjak, Heat transfer coefficient, pressure drop, and flow patterns of R1234ze(E)evaporating in microchannel tube, Int. J. Heat Mass Transf. 138 (2019) 1368–1386.
[34] M.G. Cooper, Heat flow rates in saturated nucleate pool boiling-a wide-ranging examination using reduced properties, Adv. Heat Transf. 16 (1984) 157–239.
[35] D. Gorenflo, D. Kenning, H2 pool boiling, in: VDI Heat Atlas, 2016, pp. 757–792.
[36] F. Hou, H. Zhang, D. Huang, J. Fan, F. Liu, T. Lin, L. Cao, X. Fan, B. Ferreira, G. Zhang, Microchannel thermal management system with two-phase flow for power electronics over 500 W/cm2 heat dissipation, IEEE Trans. Power Electron. 35 (2020) 10592–10600.
[37] Y. Fang, W. Yang, D. Xu, L. Hu, L. Su, Y. Huang, Experimental investigation on flow boiling characteristics of R1233zd (e) in a parallel mini-channel heat sink for the application in battery thermal management, Int. J. Heat Mass Transf. 178 (2021).
[38] Z. Rui, F. Zhao, H. Sun, L. Sun, H. Peng, Experimental research on flow boiling thermal-hydraulic characteristics in novel microchannels, Exp. Therm. Fluid Sci. 140 (2023).
[39] Q. Yang, J. Zhao, Y. Huang, X. Zhu, W. Fu, C. Li, J. Miao, A diamond made microchannel heat sink for high-density heat flux dissipation, Appl. Therm. Eng. 158 (2019).
[40] B. Agostini, R. Revellin, J.R. Thome, M. Fabbri, B. Michel, D. Calmi, U. Kloter, High heat flux flow boiling in silicon multi-microchannels–part III: saturated critical heat flux of r236fa and two-phase pressure drops, Int. J. Heat Mass Transf. 51 (2008) 5426–5442.
[41] T. Harirchian, S.V. Garimella, Microchannel size effects on local flow boiling heat transfer to a dielectric fluid, Int. J. Heat Mass Transf. 51 (2008) 3724–3735.
[42] D. Chisholm, Pressure gradients due to friction during the flow of evaporating two-phase mixtures in smooth tubes and channels, Int. J. Heat Mass Transf. 16 (1973) 347–358.
[43] A.H. Al-Zaidi, M.M. Mahmoud, T.G. Karayiannis, Flow boiling of HFE-7100 in microchannels: experimental study and comparison with correlations, Int. J. Heat Mass Transf. 140 (2019) 100–128.
[44] K. Mishima, T. Hibiki, Some characteristics of air-water two-phase flow in small diameter vertical tubes, Int. J. Multiph. Flow 22 (1996) 703–712.
[45] C. Keepaiboon, P. Thiangtham, O. Mahian, A.S. Dalkılıç, S. Wongwises, Pressure drop characteristics of r134a during flow boiling in a single rectangular microchannel, Int. Commun. Heat Mass Transf. 71 (2016) 245–253.
[46] V.Y. Lee, T.G. Karayiannis, Effect of inlet subcooling on flow boiling in microchannels, Appl. Therm. Eng. 181 (2020).
[47] Z. Anwar, B. Palm, R. Khodabandeh, Flow boiling heat transfer, pressure drop and dryout characteristics of R1234yf: experimental results and predictions, Exp. Therm. Fluid Sci. 66 (2015) 137–149.
[48] M. Zhang, R.L. Webb, Correlation of two-phase friction for refrigerants in small-diameter tubes, Exp. Therm. Fluid Sci. 25 (2001) 131–139.
[49] L. Friedel, Improved friction pressure drop correlations for horizontal and vertical two-phase pipe flow, in: European Two-Phase Flow Group Meeting, Ispra, Italy, 1979.
[50] E.R. Dario, J.C. Passos, M.L.S. Simón, L. Tadrist, Pressure drop during flow boiling inside parallel microchannels, Int. J. Refrig. 72 (2016) 111–123.
[51] H. Müller-Steinhagen, K. Heck, A simple friction pressure drop correlation for two-phase flow in pipes, Chem. Eng. Process.: Process Intensif. 20 (1986) 297–308.
[52] G. Criscuolo, W.B. Markussen, K.E. Meyer, M.R. Kærn, High heat flux flow boiling of R1234yf, R1234ze (e) and R134a in high aspect ratio microchannels, Int. J. Heat Mass Transf. 186 (2022) 122215.
[53] G. Criscuolo, W. Brix Markussen, K.E. Meyer, B. Palm, M. Ryhl Kærn, Experimental characterization of the heat transfer in multi-microchannel heat sinks for two-phase cooling of power electronics, Fluids 6 (2021) 55.
[54] S. Szczukiewicz, N. Borhani, J.R. Thome, Two-phase heat transfer and high-speed visualization of refrigerant flows in 100 × 100 μm2 silicon multi-microchannels, Int. J. Refrig. 36 (2013) 402–413.
[55] P.L. Young, T.P. Brackbill, S.G. Kandlikar, Estimating roughness parameters resulting from various machining techniques for fluid flow applications, in: Proceedings of the 5th International Conference on Nanochannels, Microchannels and Minichannels, 2007, pp. 827–836.
[56] T.Y. Chalfi, S.M. Ghiaasiaan, Pressure drop caused by flow area changes in capillaries under low flow conditions, Int. J. Multiph. Flow 34 (2008) 2–12.
[57] F. Dittus, L. Boelter, Heat transfer in automobile radiators of the tubular type, Int. Commun. Heat Mass Transf. 12 (1985) 3–22.
[58] S. Kline, F. McClintock, Describing uncertainties in singlesample experiments, Mech. Eng. 75 (1953) 38.
[59] M.R. Kærn, G. Criscuolo, K.E. Meyer, W.B. Markussen, Critical heat flux characteristics of R1234yf, R1234ze(E) and R134a during saturated flow boiling in narrow high aspect ratio microchannels, Int. J. Heat Mass Transf. 180 (2021).
[60] R. Shah, A. London, Laminar flow forced convection in ducts - chapter XVII, 1978, pp. 196–222.
[61] C. Falsetti, M. Magnini, J.R. Thome, Flow boiling heat transfer and pressure drops of R1234ze(E) in a silicon micro-pin fin evaporator, J. Electron. Packag., Trans. ASME 139 (2017).

[62] H. Huang, J.R. Thome, An experimental study on flow boiling pressure drop in multi-microchannel evaporators with different refrigerants, Exp. Therm. Fluid Sci. 80 (2017) 391–407.
[63] G. Ribatski, L. Wojtan, J.R. Thome, An analysis of experimental data and prediction methods for two-phase frictional pressure drop and flow boiling heat transfer in micro-scale channels, Exp. Therm. Fluid Sci. 31 (2006) 1–19.
[64] M.M. Mahmoud, T.G. Karayiannis, Heat transfer correlation for flow boiling in small to micro tubes, Int. J. Heat Mass Transf. 66 (2013) 553–574.
[65] S.G. Kandlikar, Fundamental issues related to flow boiling in minichannels and microchannels, Exp. Therm. Fluid Sci. 26 (2002) 389–407.
[66] S.-M. Kim, I. Mudawar, Universal approach to predicting two-phase frictional pressure drop for mini/micro-channel saturated flow boiling, Int. J. Heat Mass Transf. 58 (2013) 718–734.
[67] T.G. Karayiannis, M.M. Mahmoud, D.B. Kenning, A study of discrepancies in flow boiling results in small to microdiameter metallic tubes, Exp. Therm. Fluid Sci. 36 (2012) 126–142.
[68] S.M. Kim, I. Mudawar, Universal approach to predicting saturated flow boiling heat transfer in mini/micro-channels – part II. Two-phase heat transfer coefficient, Int. J. Heat Mass Transf. 64 (2013) 1239–1256.